



Fachbereich Biologie / Chemie
Institut für Chemie neuer Materialien

Dissertation

Zur Erlangung des Grades eines Doktors der Naturwissenschaften

– Dr. rer. nat. –

**Organometallic Polymer - Graphene
Nanocomposites: Promising Battery Materials**

vorgelegt von

Seyyed Mohsen Beladi Mousavi

Osnabrück 2016

This doctoral thesis was carried out at the Institut für Chemie neuer Materialien, Fachbereiche Biologie / Chemie, Universität Osnabrück, Germany, under the supervision of Prof. Dr. Lorenz Walder. The studies were performed in the period from Feb. 2012 to Nov. 2016.

Hauptberichterstatter: Prof. Dr. Lorenz Walder, Universität Osnabrück

Zweitberichterstatter: Prof. Dr. Martin Steinhart, Universität Osnabrück

Weitere Mitglieder: Prof. Dr. Markus Haase and Dr. Ulrich Wahlbrink
Universität Osnabrück

This thesis is dedicated to my mom and dad

Acknowledgments

First and foremost, I would like to express my sincere gratitude to my advisor Prof. Lorenz Walder for the continuous support of my research. His patience, motivation and immense knowledge added considerably to my graduate experience. I appreciate all his contributions of time and ideas to make my Ph.D. experience productive and stimulating.

Besides my advisor, I would like to thank the rest of my thesis committee: Prof. Dr. Martin Steinhart, Prof. Dr. Markus Haase, and Dr. Karsten Kömpe for their encouragement, and insightful comments.

I thank my fellow labmates: Dr. Liang Cheng Cao, Dr. Veronica-Alina Constantin, Shamaila Sadaf, Marco Schleutker, Patrick Harpel, Sascha Dumstorff, Jonas Klein, Masih Bahar, Arsalan Mahmood and Ann-Kristin Hennecke for the stimulating discussions, for the late evenings we were working together, and for all the fun we have had in the last few years. In particular, I am grateful to Mrs. Simona Webersinn and Mrs. Christine Schulz-Kölbel for the friendly environment in the lab and their continued support regarding the laboratory and administrative works.

My special thanks go to my friends Hamid Asiayee, Mariam Hosseini, Behnam Abbasi, Dr. Marius Ciobanu, Audrey Bonvin, Dr. Ana Maria Lepadatu, Pierre Bonifait, Ioana Ciupitu, Alex Ciupitu, Bárbara Rotstein, Xihomara Casallas, Martin Frosinn, Nadine Diek, Ali Arabi and Davood Gheydari for their continuous support and all the great time, we spent together during the course of this study.

I would like to thank Miriam for her understanding and constant support, which did not let me feel homesick.

Finally, but by no means least, thanks go to my loving mom and dad, and my brothers Saeed, Vahid and Davood for providing me with unfailing support and continuous encouragement throughout my years of study and through the process of researching and writing this thesis. This accomplishment would not have been possible without them.

Thank you very much, everyone!

Osnabrück, November 21, 2016.

Mohsen

Table of Contents

Thesis abstract.....	1
Chapter 1. Introduction.....	2
1.1. Battery materials: Inorganic versus organic.....	3
1.2. Organic battery materials.....	4
1.3. Advantages and challenges of organic electrodes.....	7
1.4. Motivations and methods of the present thesis.....	10
Chapter 2. Poly(vinylferrocene) - Reduced Graphene Oxide as a High Power / High Capacity Cathodic Battery Material.....	15
2.1. Overview.....	15
2.2. Introduction.....	17
2.3. Formation and characterization of PVFc@GO supramolecular complex.....	20
2.3.1. Introduction.....	20
2.3.2. Method: zeta potential.....	21
2.3.3. Experimental section.....	24
2.3.3.1. <i>Instruments</i>	24
2.3.3.2. <i>Chemicals</i>	24
2.3.3.3. <i>Oxidation of poly(vinylferrocene) (PVFc)</i>	25
2.3.3.4. <i>Zeta potential measurements</i>	27
2.3.3.5. <i>Modeling</i>	28
2.3.3.6. <i>Atomic Force Microscopy (AFM)</i>	28
2.3.4. Results and Discussion.....	28
2.3.4.1. <i>Zeta potential measurement</i>	28
2.3.4.2. <i>UV-Vis measurement</i>	30
2.3.4.3. <i>Molecular modeling</i>	31
2.3.4.4. <i>Morphology of PVFc@GO complex in dry state</i>	33
2.3.5. Summary.....	35
2.4. Electrocatalytic transformation of (PVFc@GO) _n @CC to (PVFc@rGO) _n @CC by viologen.....	37
2.4.1. Introduction.....	37
2.4.2. Experimental section.....	38
2.4.2.1. <i>Instruments</i>	38
2.4.2.2. <i>Chemicals</i>	39

2.4.2.3. Preparation of PVFc@GO solutions with varying PVFc ^{x+} / GO ^{m-} ratio	39
2.4.2.4. Electrochemical measurements and electrode preparation	40
2.4.2.5. Electrochemical transformation of (PVFc@GO) _n @CC to (PVFc@rGO) _n @CC	40
2.4.2.6. Electrochemical Quartz Crystal Microbalance (EQCM)	40
2.4.2.7. Conductivity	41
2.4.2.8. Raman spectroscopy	41
2.4.2.9. Electrochemical AFM	42
2.4.3. Results and Discussion	42
2.4.3.1. Cyclic voltammetry	44
2.4.3.2. EQCM	48
2.4.3.3. Electrochemical-AFM	51
2.4.3.4. Raman spectroscopy	56
2.4.3.5. Thermogravimetric analysis	56
2.4.3.6. Electrical conductivity	57
2.4.4. Summary	57
2.5. Energy Storage Performances	59
2.5.1. Introduction	59
2.5.2. Experimental	60
2.5.2.1. Instruments	60
2.5.2.2. Chemicals	60
2.5.2.3. Battery performance tests	60
2.5.3. Results and discussion	60
2.5.4. Summary	65
Chapter 3. Summary and Outlook	67
3.1. Summary	67
3.2. Outlook	70
References	71
Abbreviation	74
Curriculum Vitae	75
Declaration	76

Thesis abstract

Preparation, structural analysis, and electrochemical performance of a new cathodic battery material, consisting of a nanocomposite of poly(vinylferrocene) (PVFc) (E_{ox} : 0.4 V vs. Ag/AgCl) and reduced graphene oxide (rGO), are described. The nanocomposite shows the highest charge-discharge efficiency (at a rate of 100 A g⁻¹) ever reported for any organic / organometallic battery material. Remarkably, the composite is “thickness scalable” up to 0.21 mAh cm⁻² (770 mC cm⁻² at 29 μm film thickness) on a flat surface with > 99% coulombic efficiency, exhibiting a specific capacity density of 114 mAh g⁻¹. The composite material is binder free and the charge storing material (PVFc) accounts for > 88% of the total weight of the cathodic material. The secret behind such a performance is the electrostatic interaction between the redox polymer in its oxidized state (exhibiting positive charge) and the original filler i.e., graphene oxide (GO) with negative surface charge. This self-assembling step is analyzed by zeta potential measurements, and a modeling study confirms the experimentally found heavy polymer loading on the GO (in aqueous solution). The efficient self-assembly led to composites with high ratio of redox polymer / GO where all polymers are in close contact with GO sheets. The stable colloidal solution was casted on the surface of a flat current collector and the insulating GO was electrochemically transformed to conductive reduced graphene oxide (rGO). The GO / rGO transformation was catalyzed by methyl viologen dichloride (MV⁺⁺) working as a redox shuttle (solubilized in the aqueous electrolyte) and thereby accelerating the electron transfer to GO. Complete GO / rGO transformation and the quantitative ion breathing of the composite are found by means of electrochemical quartz crystal microbalance and electrochemical AFM. Further work in the field was done, but as it is part of a pendant patent application, will not be mentioned in this thesis.

Chapter 1

Introduction

Burning fossil fuels and biomass are the most known energy sources, which are widely used for different applications. However, the unavoidable subsequent gas emission causes environmental pollution and results in global warming, which could have problematic consequences. Moreover, these resources are non-renewable. On the contrary, the green energy sources such as solar radiation, wind, and waves are renewable. However the limitation in time and place of energy generation of renewable sources clearly indicates their dependency on energy carriers and / or energy storages. Energy carriers are the electricity grid, electromagnetic waves, chemical energy and batteries. The latter two are “portable energy sources”. However, batteries, in contrast to fossil fuels, can convert stored chemical energy to electrical energy with a high efficiency and additionally do not produce gaseous exhaust. The portable energy storages are crucial in the modern mobile society for many applications ranging from small scale energy storages such as cellular telephones, smart watches and laptops to bigger scales such as electrical vehicles.¹

Each cell of a battery consists of a cathode (reductant) and an anode (oxidant), that are separated by the electrolyte, which transfers ions during the electrochemical reaction inside the active battery materials. During a discharge cycle, two reversible electrochemical reactions, an oxidation and a reduction, happen in the two battery materials, the anode and the cathode, respectively. An external current (I) over a specific time (Δt) at a voltage (V) is provided. The difference between the redox potentials of the anode and the cathode is the theoretical voltage ($V [V]$) of the battery. In order to prevent the irreversible oxidation / reduction of the electrolyte, the redox potential of anodes and cathodes of a thermodynamically stable battery have to be between the LUMO and the HOMO of the electrolyte i.e., the electrolyte window (**Figure 1.1**). The electrolyte window of the aqueous electrolyte is limited to max. 1.23 V, while it is > 3 V in organic solvents.²

An ideal battery can provide a high energy density (Wh kg^{-1}) in a short time ($> 5\text{C}$) as well as in a given volume (mAh cm^{-3}), surface (mAh cm^{-2}) or mass (mAh g^{-1}). In addition, cost, safety, an environmentally friendly operation and cyclability are also crucial factors, which should be respected in the developments of new battery materials. The specific capacity (mAh g^{-1}) and energy density (Wh kg^{-1} : specific capacity (Ah kg^{-1}) \times nominal battery voltage (V)) are dictated by the nature of the redox materials. In contrast to that, the volumetric capacity (mAh cm^{-3}), areal-capacity (mAh cm^{-2}), and charging-discharging rates (also depended on the redox material) are additionally controlled by the electrode design.

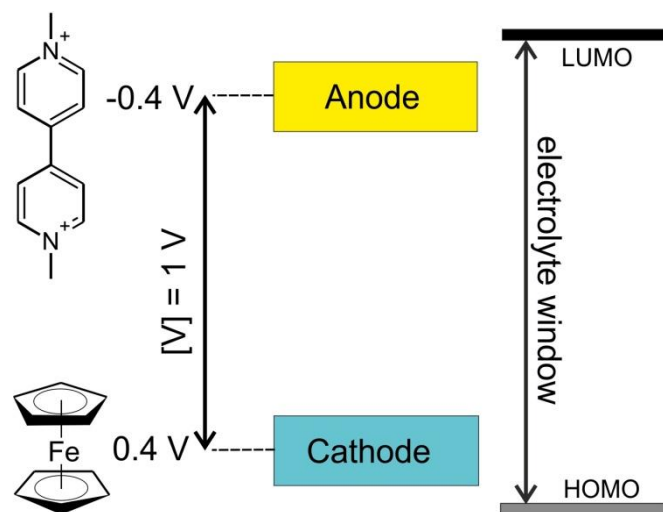


Figure 1.1 Schematic open-circuit energy diagram of an electrolyte. Anode: dimethyl viologen (MV^{++}) and cathode: ferrocene.

1.1. Battery materials: Inorganic versus organic

Since the early 1990, the portable battery market is dominated by lithium – ion batteries (LIBs) due to their high energy density. A conventional LIB consists of graphite or other carbon materials as an anode and a stable intercalated framework as a cathode, which can reversibly host the lithium ions. The crystalline structure of the framework in conventional cathode materials is mostly based on transition metals or phosphates such as LiCoO_2 , LiMn_2O_4 , or LiFePO_4 . These frameworks restrict the theoretical capacity of LIBs to $\sim 180 \text{ mAh g}^{-1}$, although the anode materials can provide the gravimetric capacities

$> 1000 \text{ mAh g}^{-1}$.³ Hence, many researches are still concerned with developing novel, high capacity cathode materials for conventional LIBs, e.g., vanadium-oxide based batteries with theoretical capacity $> 400 \text{ mAh g}^{-1}$ (However, their capacities are depended on many redox states (V^{2+} to V^{5+}) in a broad potential range ($> 2\text{V}$)⁴ and additionally they have a short cycle life).

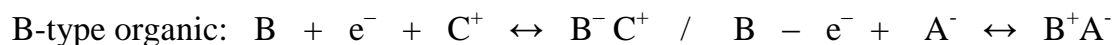
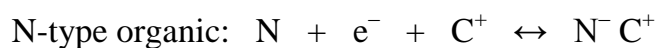
In conventional LIBs, the rate of the (de)intercalation of Li-ions is mainly limited by the diffusion of Li-ions into the crystalline cathodic host structure. Smaller crystals provide shorter paths; however, the syntheses of the small crystals are often very expensive. Moreover, there are still serious safety concerns due to the unwanted reaction between the electrode materials and the electrolyte (i) and the flammability of the organic electrolyte (ii). Some other essential requirements for today's market related to Internet of Things (IoT) are still not easily feasible with classical LIBs, such as flexibility, long cycle life, efficient processing e.g., spraying and roll to roll, efficient operation in aqueous electrolyte and absence of toxic and non-renewable materials. This has triggered considerable research attention toward more advanced battery materials such as Li-O₂, Li-S and Li-organic batteries. Interestingly, the research and industrial attention towards organic materials for energy storage application, as compared to inorganic electrodes is negligible. This is historically due to the fast developments of LIBs. However, the use of organic or organometallic redox compounds could overcome many of the mentioned problems of the LIBs, as it will be discussed in the following sections.

1.2. Organic battery materials

A reversible electrochemical redox reaction is the first requirement for any electrode material candidate to be used as an anode or cathode. Elemental substances (e.g., Li, Na, C, O₂, S, Si, P, Sn, I₂), transitional metals (e.g., Co, Mn, V, Ti, Fe, Ni), and organic materials (monomers, oligomers, dendrimers and polymers) are theoretically possible candidates for secondary batteries. Redox active organic molecules consist

usually of a π -conjugated structure and atoms with lone pair electrons such as O, N and S. The conjugated structure accelerates the charge delocalization of the redox product.⁵ In other cases e.g. in the case of Tempo, the electrophore is localized and tert. butyl groups protect the radical from dimerization. As well known from Marcus-Hush theory, the kinetics of a reversible redox reaction of organic molecules depend on the reaction mechanism, e.g., in a disulfide, the reductive breaking of the S-S bond and its oxidative formation from two S^- is slow and needs therefore a high activation energy. Bond breaking and bond formation is obviously not involved in the redox processes of a tempo radical, viologen or ferrocene and fast kinetics are therefore expected. Anyhow, the electron transfer is not the only possible rate determining step, it can as well be the movement of counterions.

The redox reaction of an organic electrode is based on the reversible redox reaction of the organic functional groups:



while N = neutral state of n-type organic, P = neutral state of p-type organic, B = neutral state of bipolar organic, C = cations, e.g., H^+ , Li^+ , Na^+ , B^+ , NH_4^+ and etc, and A = anions e.g., Cl^- , Br^- , I^- , ClO_4^- , PF_6^- and etc. The cathodic materials in LIBs are limited to the specific radius of Li^+ . However, in n-type or p-type redox organic material, replacing counterions, do not essentially affect the electrochemical responses.

Some examples of well-known organic electroactive groups, based on their redox reaction potentials, are summarized in the **Figure 1.2**. A totally organic battery is based on the combination of a cathode with the higher redox potential e.g., 1,4-Di-t-Butyl-2,5-dimethoxybenzene (Figure 2.1.a) ($E^0 = 1.2 \text{ V vs. Ag/AgCl}$) and an anode with the lower redox potential e.g., disulfide (Figure 2.1.i) ($E^0 = -1.2 \text{ V vs. Ag/AgCl}$), which, in this case, provide a 2.4 V cell. However, the organic electrodes are often used as cathode

materials in combination with inorganic anode material e.g., lithium. For instance, the combination of Ferrocene / Li provide a ~3.7 V battery (Li / Li⁺ is -3.26 vs. Ag/AgCl).

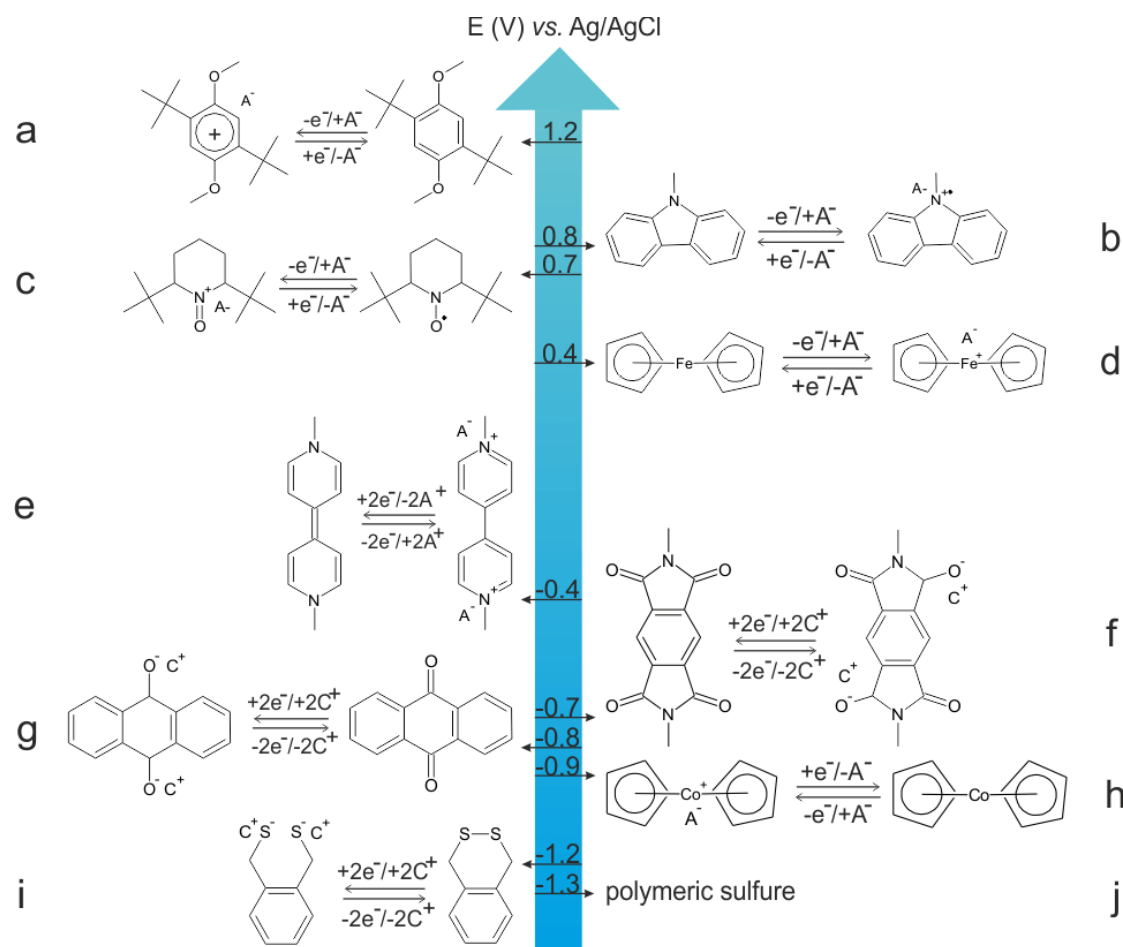
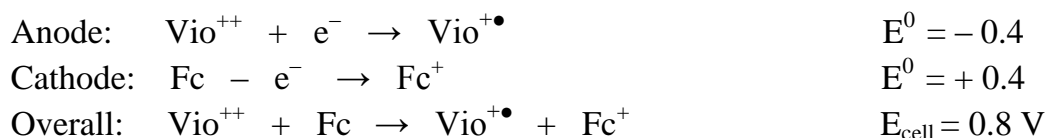


Figure 1.2. Redox potentials of some well-known electroactive organic molecules. (Li/Li⁺ is -3.26 vs. Ag/AgCl); a) 1,4-Di-*t*-Butyl-2,5-dimethoxybenzene, b) 9-Methylcarbazole, c) (2,2,6,6-Tetramethylpiperidin-1-yl)oxyl (TEMPO), d) Ferrocene, e) Dimethyviologen, f) 2,6-Dimethylpyrrolo[3,4-*f*]isoindole-1,3,5,7(2H,6H)-tetrone, g) Anthraquinone, h) Cobaltocenium, i) (α,α' -dithio-*o*-xylene), j) Polymeric sulfure.

A pure organic battery using a viologen polymer as anode and a ferrocene-based polymer as cathode is shown in **Figure 1.3**. The reaction mechanism during charging is as below:



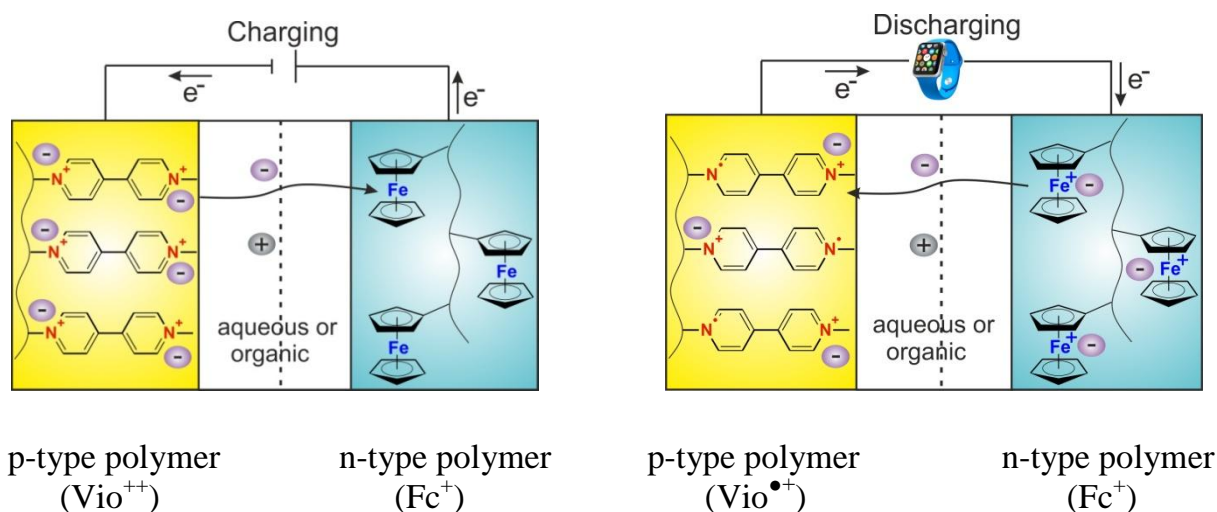


Figure 1.3. Schematic representation of an organic battery consisting of a poly-Viologen (yellow) as the anode and a poly-Ferrocene polymer (blue) as the cathode during charging and discharging cycles.

1.3. Advantages and challenges of organic electrodes

Typical key words used in battery research are presented here. The content describes shortly the properties of the redox polymer battery materials in comparison with inorganic battery materials with respect to the key words:

High Power density ($W\ kg^{-1}$): power density is depended on both, the electrochemical reaction mechanism and the electrode design (an adequate percolation system). In the conventional LIBs, the observed rate is limited by the slow (de)intercalation of the lithium ions in the host lattice of the metal oxide cathode. Organic charge storing materials may exhibit very fast hetero- and homogeneous E.T. rates e.g., tempo, ferrocene and viologen. For fast redox systems, kinetic limitations are usually caused by another step in the complete systems, e.g. from ion movement or electronic conductivity in the battery material. Perfect percolation systems throughout the electrode material, which allow fast ion and electron movements, is needed to observe fast redox systems in high power organic / inorganic electrodes.⁶

High energy density ($Wh\ kg^{-1} = 3600\ J\ kg^{-1} = cell\ potential\ (V) \times specific\ capacity\ (Ah\ kg^{-1})$): the cell voltage of commercial Li-intercalation-based cathode / -anode systems

can deliver > 3.5 V, a value higher than most organic materials / Li combinations, and not attainable by any organic / organic systems. However, organic materials can achieve higher capacities compared to traditional LIBs (with maximum specific capacities of 180 mAh g^{-1}) and this can compensate the lower voltage of organic systems. For example, the theoretical energy density of dimethyl viologen is $\sim 820 \text{ Wh kg}^{-1}$ (theoretical capacity $= 288 \text{ mAh g}^{-1} \times \text{redox potential versus Li} = 2.86 \text{ V}$), which is therefore higher than the one of the established Li / LiCoO_2 , $\sim 550 \text{ Wh kg}^{-1}$.⁷

Dissolution: the dissolution of molecular organic redox material during the charging-discharging process is a big drawback, which finally results in a low cyclability. The use of polymeric organic electrophores can circumvent this problem.

Intercalation: In the case of inorganic electroactive metal oxides or phosphates with crystalline fixed places, Li^+ ions (de-)intercalate between the lattice layers to compensate the charge introduced by oxidation / reduction. In the case of an electroactive redox polymer the subunits are generally amorphous and Li ions percolate within an organic porous system for charge compensation of the redox subunits. The rigid crystalline host is structurally restrained and does not change its shape during an oxidation / reduction cycle, but in contrast to this, the organic or organometallic redox polymer can adopt its best conformation during the redox process, leading generally to a thickness change, a phenomenon described as “breathing”.

Structure redox tuning: The search for new types of inorganic materials has not been very successful in recent years in spite of a huge amount of research invested in this field, but mainly focused on a few structures. I believe that the synthesis of novel organic redox polymers with optimized properties has a bigger chance to deliver useful compounds because the synthetic variability is much larger than in the case of inorganic materials. Effectively, the electrophores shown in Figure 1.2 is only a small non-representative selection of possibilities.⁸

Low volumetric mass density (mAh cm^{-3}): the mass density of organic redox materials is lower ($1\text{--}1.5 \text{ g cm}^{-3}$) than that one of inorganic ones (CoO_2 : 6.4 g/cm^3 , LiFePO_4 : 3.6 g cm^{-3}). This is due to heavy elements content and dens crystalline state of inorganic materials. In devices, in which only high gravimetric density counts, this will not considered as a disadvantage of the redox polymers, however, the volumetric energy may play a role for applications with restricted place available, i.e. for smart watches, mobile phones and electric vehicle.

Environmentally friendly: the finite resources of transition metals, their expensive synthesis and recycling, as well as the danger of environmental pollution, if they are not recycled, lead to the conclusion, that traditional LIBs are not sustainable. On the contrary, organic redox materials can principally be prepared by synthesis from biomass, and they are recyclable via the natural carbon dioxide cycle. Thus, redox polymers can be considered as CO_2 neutral.

Flexibility: Amorphous redox polymers are – in contrast to metal oxides or phosphates - naturally flexible, and thus, allow principally the production of thin and wearable batteries.

Low electronic conductivity: The single charge storing sites in a battery material need to be able to exchange electrons with each other, according to either a band structure model for crystalline solids, e.g. LiFePO_4 or a backbone-poly thiophene, or according to an electron hopping mechanism as for example for poly-Ferrocene. The charge propagation mechanism has been discussed thoroughly in literature. It is absolutely not trivial to distinguish limitations set by the electron propagation and those set by the counterion movement. The addition of large amounts of conductive carbon is used to increase the conductivity. However, this technique results in a lower specific capacity. Due to the low mass density and high surface area of the organic compounds, a larger amount of conductive carbon is necessary for organic redox materials compared to crystalline inorganic materials.

Cheap: the organic electrode materials that may be principally prepared from biomass sources are cheap and in contrast to LIBs, recycling is not necessary.

1.4. Motivations and methods of the present thesis

The main goal of the current thesis is to overcome the known limitations of the organic electrodes such as low cyclability and low areal-capacity, and taking advantage of the organic material's high power-density. Small redox organic materials suffer from easy dissolution in the electrolyte upon charging-discharging. This results in a fast loss of capacity. Moreover, the dissolved molecules can shuttle between electrodes, which results in self-discharging of the battery. The synthesis of polymeric redox material has been shown as a reliable method to overcome the dissolution problem. However, considering theoretical application, a simple synthesis route and choose of cheap raw materials are crucial.

The factors influencing the areal-capacity (mAh cm^{-2}) are the theoretical capacity of the redox material ($C_{\text{theoretical}}$, mAh g^{-1}) and the construction of excellent percolation paths for ions and electrons in the thick layers. The molecular weight of the organic molecule (M_w), which stabilizes the redox active unit and the number of redox states (n) are important factors in the theoretical capacity of the redox molecule:

$$C_{\text{theoretical}} = \frac{n \times F}{M_w} = \frac{n \times 96485 \left(\frac{\text{As}}{\text{mol}}\right)}{M_w \left(\frac{\text{g}}{\text{mol}}\right)} = \frac{n \times 26801}{M_w} \left(\frac{\text{mAh}}{\text{g}}\right) \quad \text{Eq. 1.1}$$

where n is the number of involved electrons, F the Faraday constant, and M_w the molar mass of the redox unit. The theoretical capacity can be increased by the synthesis of redox organic units with low molar mass or by enabling a multi-redox reaction on one unit. An excellent electronic and ionic conductivity of the active layer are also crucial factors for the preparation of high areal capacity electrodes. Redox polymers have no / little electronic conductivity (except conducting polymers e.g., polyaniline, which suffer from

low theoretical capacity), which limits their performance for battery application. There have been many methods proposed to overcome this problem e.g., drop casting a thin layer of polymer on the current collector;⁹ electropolymerization on the surface of electrode,¹⁰⁻¹¹ spin-coating¹² and others. The data obtained by electrochemical measurements such as diffusion coefficient and electron transfer rate showed that in films thicker than 200 nm ionic and electronic conductivity are limiting factors, which decrease the electrode performance. Therefore, there have been many methods suggested to defeat this problem. The synthesis of composites based on redox polymers / conductive fillers is a known method, which is widely used, even in the state of the art of Li-ion¹³ and Li-S¹⁴ batteries. The conductive fillers are mainly nanostructured carbon materials e.g., graphite and carbon nanotube. The addition of conductive polymers is also known, however, these polymers are – in contrary to conductive carbons - just conductive in a specific potential range (their doped state), which limits their application. Insertion of conductive carbon in the polymer matrix provides conductivity throughout the composite, which accelerate the electron / ion transfer from the current collector to the redox sites and vice versa. A high rate response can be achieved when the redox sites are in direct / close contact to the conductive fillers to enable a barrier-free electron transport. In addition to electron conductivity, ionic conductivity is also an important factor in a fast charge-discharge process. This is achieved through a porous system, which is mechanically stable after several penetration / de-penetration cycles of electrolyte. It is reported that the necessary amount of conductive additive in the polymers with large aromatic backbone such as poly-Imides¹⁵ or poly-Anhydrides¹⁶ are less than in non-aromatic polymers. Electron-hopping in non-aromatic polymers such as poly-Tempo and poly-Ferrocene also decreases the necessary amount of conductive fillers.¹⁷ Anyway, addition of a large quantity of conductive fillers (40-90 w% of the composite weight) to the redox organic materials is necessary, which results in a considerable capacity loss of the composite. This is probably due to the high surface area of organic materials. Hence, it is crucial to develop the polymer-filler composites using the least amount of fillers with high utilization of redox materials and considerably enhanced electrochemical response.¹⁸ Moreover, this

composite materials have to be scalable i. e., keep the high electrochemical performance in the layers with thicknesses $> 20 \mu\text{m}$.

Recent studies on nanocomposites have shown that addition of 2% nanofillers e.g., exfoliated nanoclays¹⁹ and graphite nanoplatelets²⁰ into the polymer matrix can dramatically change the polymer's properties. Beside the inherent properties of the nanofiller, taking advantage of the high surface area of the nanofiller by optimizing the dispersion quality, interface chemistry and nanoscale morphology have significant effect on the polymer properties. The enormous interfacial area provided by well-dispersed nanoparticles could affect the behavior of polymer matrix for several radii of gyration.²¹ Exfoliated graphite nano-platelets, carbon nanotubes and amorphous carbon have high surface area. The highest electronic conductivity per mass and the highest surface to volume ratio can be achieved by interconnected single graphene sheets, which are in close contact with the redox active polymers. Graphene has already been used for the development of battery materials,^{6, 18} electrochromic devices,²² sensors,²³ perovskite solar cells²⁴⁻²⁵ and others. Although graphene can provide a high surface area, it suffers from low solubility in organic and aqueous media. This hampers the intended tight contact between graphene single sheets and the polymer during synthesis and leads to phase separation preventing the construction of the electron and / or ion percolating system on a nanometer scale.²⁶ In other words, strong interaction between the carbon fillers e.g., graphene or CNT and the redox polymers is a vital step towards tight contact and this implies homogeneous dispersions of the partners prior to contact and high affinity between components after contact. Well-dispersed carbon-based filler provides higher surface areas and that results in more efficient neighboring interaction upon contact with the polymer chains based inter alia on π - π stacking interaction,²⁷ but the same type of interaction makes it difficult to disperse e.g., graphene prior to contact with the polymer. On the other hand, graphene oxide (GO), synthesized by chemical oxidation of graphite,²⁸ or partially oxidized CNTs are bearing many oxygen-containing functional groups (hydroxyl and epoxide functional groups on the basal plane of the sheets and carbonyl and carboxyl groups at the sheet or tube edges), which make the $\sim 1\text{nm}$ -thick-GO sheets and

tubes hydrophilic and therefore readily dispersible in polar solvents.²⁸ For the last part of the introduction the focus will be exclusively on GO, but the arguments for oxidized CNTs are similar. Notably, the negative surface charge of GO prevents the association of single GO sheets with each other, but it allows for self-assembling of individual GO sheets with poly cationic polymers e.g., polyethyleneimine²⁹ and poly(1-vinyl-3-ethylimidazolium)bromide³⁰. The efficient interaction of positively charged polymers with negatively charged, individual GO sheets allows the preparation of suspensions with high polymerⁿ⁺ / GO^{m-} ratios, in which polymers are in direct / close contact to individual GO sheets. Other reports also show electrostatic interaction of bio-molecules such as peptides, proteins and amino acids³¹⁻³² with GO sheets. In case of electroactive polymers, it may be sufficient to oxidize them partially in order to generate polymerⁿ⁺ and to achieve molecular wrapping, in other cases the positive charges have to be introduced on purpose synthetically (**Figure 1.4**).

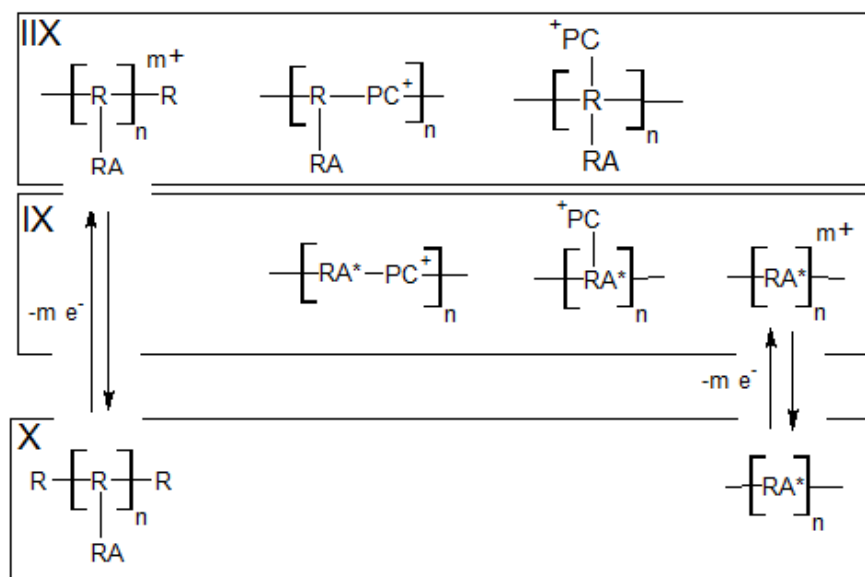


Figure 1.4. Preparation of polycationic redox polymer for self-assembly on GO. Upper box: polymers with a redox active (RA) unit in the side chain in the oxidized state. Middle box: polymers with redox active units in the main chain in the oxidized state. L: polymers where the side or main chain is in the neutral state, which upon partial oxidation is transferable to a or b. R: non-redox-active subunit chains; RA: electroactive side chain subunit; RA*: electroactive main chain subunit; PC⁺: persistent positively charged subunit; n: number of subunits in the polymer; m⁰: number of persistent charges generated by (partial) oxidation of RA or RA*, where m⁺ ≤ n.

In any case, if the wrapping is perfect, the distance between GO and the redox centers is small, thus, electron transfer between GO in a conductive form and the polymeric redox centers is possible. The surface of GO, depending on the polymer / GO ratio, can be covered by a single or by multiple layers of the polymer. The specific capacities at large current densities are tunable by the optimization of polymer / GO ratio. The optimized ratio provides perfect ion and electron percolation system throughout the composite layer, which is an important goal in this thesis. GO has only a minor conductivity, but becomes conductive upon reduction.³³ It can be reduced chemically, thermally, and electrochemically to so-called "reduced graphene oxide" (rGO), a process which regenerates many sp^2 carbons at the periphery and within the plane of the original graphene network and doing so, conductivity is re-established. Chemical reduction often employs hazardous chemicals e.g., hydrazine.³⁴ Thermal reduction of GO occurs in the temperatures ($> 600^\circ\text{C}$), in which many of organic polymers are not stable.³⁵ The electrochemical reduction technique, using a surface confined graphene oxide layer on the electrode, is most adequate for GO modified electrode surfaces. The formation of a stable redox polymer / GO colloidal solution and its application onto the current collector prior to GO-rGO transition provides electrode, in which redox polymers are in contact with individual sheets of conductive fillers i.e., rGO.

Chapter 2

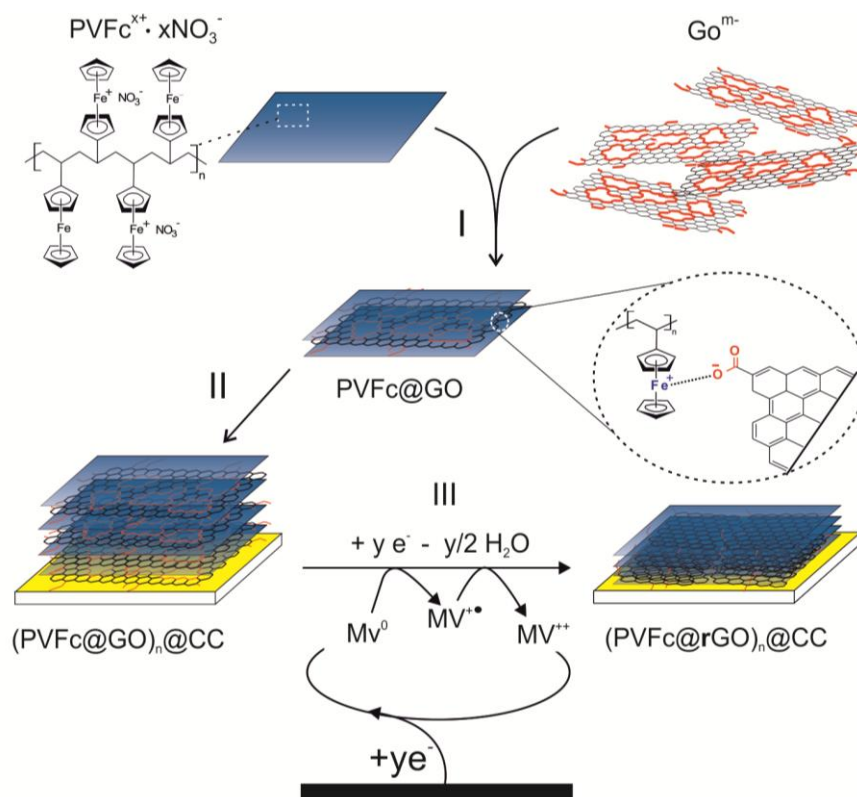
Poly(vinylferrocene) - Reduced Graphene Oxide as a High Power / High Capacity Cathodic Battery Material

Some parts of this chapter were published in “Adv. Energy Mater. 10.1002/aenm.201600108”

2.1. Overview

This Chapter is divided to 5 subchapters. After a short overview in the current subchapter on the composite preparation and the characterization methods, the next subchapter (2.2) will give an introduction on the state of the art organic battery materials with main focus on the cathodic materials such as poly-Ferrocene and poly-Tempo. The importance of using little wt% of conductive fillers is also discussed. In the subchapter 2.3, electrostatic interaction of GO and partially oxidized PVFc is investigated (Scheme 2.1 - I). Zeta potential and Vis measurements are used to characterize the supramolecular formation of PVFc@GO in the aqueous solution and atomic force microscopy (AFM) images exhibited the morphology of the composite in the dried state. In the subchapter 2.4, film formation of PVFc@GO on the current collector i.e., (PVFc@GO)@CC (Scheme 2.1 – II) and electrocatalytic transformation of (PVFc@GO)@CC to (PVFc@rGO)@CC is described (Scheme 2.1 – III). The electrocatalytic reduction is evidenced by cyclic voltammetry (CV) and electrochemical quartz crystal microbalance (EQCM). Raman measurements and a thermogravimetric method have also been used in this subchapter to show the quality of GO / rGO transformation. Furthermore, the dynamic of charging-discharging composite material on the current collector including height change and weight change using Electrochemical-AFM (EC-AFM) and EQCM, respectively, are studied. In the last subchapter (2.5), the energy storage performance of the composite material including charge-discharge rate, thickness scalability and cyclability is investigated. These measurements were performed by voltammetric and galvanostatic techniques.

In the following, I abbreviate PVFc loaded GO with PVFc@GO. Without further mention, e.g. for all of the battery performance tests, the composition indicated with a dashed square in Figure 2.5 (zeta potential = 15 mV, weight ratio = 4.4) is used. Generally, each drop (1n = 1.68 μ l, containing 0.84 μ g of PVFc (4×10^{-9} mol) and 0.19 μ g of GO) was casted on the substrate followed by drying at 50°C for 1 hour. Such casting/drying cycles were performed repetitively in case of the electrode for battery tests. The resulting surface-modified electrode is abbreviated as (PVFc@GO)_n@CC with n indicating the number of drop casting/heating cycles (1n = 1.68 μ l).



Scheme 2.1. PVFc^{x+} · xNO₃⁻: partially oxidized PVFc, see Scheme 2.2, GO^{m-}: graphene oxide (41-50 % oxygen content, zeta potential: -36.9 mV), PVFc@GO: positively charged complex in dispersion (zeta potential = +15 mV, see Figure 2.5, obtained from a weight ratio PVFc^{x+} / GO^{m-} = 4.4) (PVFc@GO)_n@CC: composite material obtained from n-fold casting / drying on a current collector (CC). (PVFc@rGO)_n@CC: reduced graphene oxide composite material on CC obtained by electrocatalytic reduction. CC: current collector (glassy carbon (GC), gold, indium tin oxide (ITO) or fluorine doped tin oxide (FTO)). I: self-assembling of PVFc^{x+} · xNO₃⁻ on GO^{m-} involving ion exchange and excessive PVFc^{x+} · xNO₃⁻ deposition on GO^{m-} (weight ratio PVFc^{x+} / GO^{m-} = 4.4) to yield PVFc@GO (zeta potential = 15 mV, see Figure 2.5). II: n-fold, drop casting and drying of PVFc@GO on current collector (CC) yielding (PVFc@GO)_n@CC (n=1: refers to each time drop casting, which produces a film containing 0.84 μ g of PVFc (4×10^{-9} mol)). III: GO→rGO reduction using electrocatalyst methylviologen (MV⁺⁺), active state: MV^{+•} and MV⁰ regenerated at the current collectors (CC) and at rGO (potential range 0 to -1.3 V vs. Ag/AgCl).

2.2. Introduction

Energy density, power density, low cost and long cycle life are the main factors for mobile battery applications.³⁶⁻³⁷ Li-ion batteries, which are based on the intercalation concept of Li^+ in the anodic and cathodic materials dominate today's rechargeable battery market for small mobile up to automotive applications. However, costs, safety concerns, restricted energy and power densities are still a problem.³⁸⁻³⁹ The Li-ion batteries' restricted energy and power density originates mainly from the cathodic battery material, consisting of a stable intercalation framework, e.g., electroactive transition-metal oxides or phosphates. Rapid charging and discharging are limited by slow (de)intercalation of lithium ions and by low electronic conductivity.

Organic materials can provide a light weight framework with a higher specific capacity as compared to inorganic materials.⁸ Their oxidation potential can be tuned by chemical synthesis and their electronic conductivity can be optimized on the molecular level. Furthermore, they are potentially cheap and recyclable.⁸ Sulfide-, free radical-, and aromatic carbonyl-based conductive or non-conductive materials, e.g. ferrocenes or viologens have been studied as organic energy storage materials.^{8, 10, 40-43}

Ferrocene-based materials have shown unique properties such as air stability, fast electrochemical kinetics and a stable voltage plateau leading to the development of the ferrocene-based reference electrode, and cathodic battery material.⁴⁴⁻⁴⁹ Moreover, ferrocene-based materials, especially side-chain attached polymeric ferrocenes, have attracted much attention in the field of "redox responsive materials / polymers" e.g. redox triggered release of a dye from patchy nanocapsules,⁵⁰ in catalysis modulation,⁵¹ for switching surface wettability,⁵² and some other applications such as memory devices, nanoparticle synthesis and permselective membrane gating.⁵³ There have been several reports on ferrocene-based polymer batteries with ferrocene either in the backbone of the polymer chain or as pendant group of the chain.^{46-47, 54-57} Side-chain ferrocene-containing polymers are electrically insulating, which limits their use as energy storage material to small thicknesses if fast charging / discharging kinetics are required. The electronic

conductivity can be enhanced by incorporation of conductive polymers / carbon materials. It has been shown that for nanocomposites, the addition of a small quantity of filler can be sufficient as long as the dispersion quality, interfacial chemistry and the nanoscale morphology are optimized.²¹ Exfoliated and well-dispersed fillers such as graphite nanoplatelets,^{20, 58} carbon nanotubes (CNTs)⁵⁹⁻⁶⁰ and nanoclays¹⁹ increase the interfacial areas, which affect the behavior of the neighboring polymer matrix to the distance of several radii of gyration.^{21, 61-62} From a theoretical perspective, the highest electronic conductivity per mass and the highest surface to area ratio can be achieved for interconnected single graphene sheets, which are in close contact with the redox polymers. However, owing to the poor solubility of graphene sheets in water and organic solvents, the preparation of graphene single sheets and their controlled molecular interaction with redox polymers is difficult.

In contrast to pristine graphite, graphite oxide is heavily oxygenated, bearing hydroxyl and epoxide functional groups on its basal planes and carbonyl and carboxylic groups on its sheet edges.⁶³⁻⁶⁴ Its hydrophilic nature allows graphite oxide to readily swell and disperse in water, producing 1nm thick graphene oxide (GO) sheets upon mild ultrasonic treatment.⁶⁵ In fact, exfoliation of graphite oxide is the most efficient way to produce suspensions of carbon sheets, making it an ideal filler for polymer nanocomposites.⁶⁶ Unlike graphite, GO is electrically insulating, which is inappropriate for conductive filler applications. Partial restoration of the extended graphitic sp^2 carbons network by different types of reduction of GO to reduced graphene oxide (rGO) is possible. The reduction can be chemical, thermal, or electrochemical with the latter reported as especially mild.⁶⁷ There are also indications in literature that viologen may electrocatalyse the reduction of GO to rGO.⁶⁸⁻⁶⁹ The reduction reestablishes electronic conductivity, but leads also to irreversible coagulation of rGO and again tight interaction of a single rGO sheets with polymer strands is difficult after the reduction step.⁶⁶ Some successful efforts have been reported to stabilize graphene or rGO in solution, for example, by chemical functionalization or by using non-covalent interaction with surfactants providing stable platelets of graphene sheets in aqueous solution.^{33, 70}

However, the weight increase introduced with such additives just for dispersibility reasons has a negative impact on the specific capacity of the final battery material. It is therefore a challenging task to find electroactive polymers able to directly disperse single sheet graphene, rGO or GO (followed by GO / rGO transformation) without the use of dispersing agents with negative ballast implications in the final composite material.

In the present chapter a way to disperse negatively charged GO single sheets with partially oxidized poly(vinylferrocene) by electrostatic interactions using polymer / GO weight ratios up to 10:1 is shown. Zeta potential measurements, electrochemical results and AFM studies show tight molecular interactions. Achieving a high weight ratio of electron storage material to conductive filler combined with excellent percolation paths for ions and electrons was a main goal of this study. It is shown that individual GO sheets are well-dispersed throughout the polymer matrix and that is achieved in the current case by supramolecular polymer-GO complex formation prior to the polymer-GO / polymer-rGO transformation. For this purpose the stable colloidal polymer-GO solution was directly deposited on the current collector, and electrochemically reduced to polymer-rGO using methyl viologen dichloride (MV^{++}) as homogenous electrocatalyst (Scheme 2.1). The reductive removal of oxygen-containing functional groups was monitored by Electrochemical Quartz Crystal Microbalance (EQCM), and the electrocatalytic role of MV^{++} was demonstrated by cyclic voltammetry (CV). Electrochemical tests have shown that after GO / rGO transformation the electronic and ionic conductivity of PVFc were significantly enhanced; e. g., a film of (PVFc@rGO)@GC with a specific capacity of 5.8 mC cm^{-2} was > 98% charged / discharged in less than 3 seconds, and increasing the layer thickness up to ca. $29 \text{ }\mu\text{m}$ yielded a capacity of 770 mC cm^{-2} accompanied by just 1% capacity fade. These values are significantly higher than previously reported nitroxide radical polymers, which provided best capacities smaller than 150 mC cm^{-2} .⁷¹⁻⁷⁴

2.3. Formation and characterization of PVFc@GO supramolecular complex

2.3.1. Introduction

A complex of molecules, which are held together by non-covalent bonds (e.g., electrostatic, H bonding or π - π interaction) is called a supramolecular assembly. The supramolecular assemblies can involve small molecules e.g., dimmers of acetic acid in the gas phase, or it can involve larger subunits to yield complexes in the nanometer to micrometer range hold together by so called weak non-covalent interactions. Based on the surface charge of all components dispersed in aqueous solution and the recalling supramolecular assembly, stable colloidal solutions can be achieved for the components as well as the supramolecular complexes.

Graphene oxide (GO) consist of aromatic graphitic domains separated by sp^3 carbons, which are decorated by oxygen-containing functional groups such as hydroxyl, epoxy and carboxylic. Hydroxyl groups of GO allows hydrogen bonds with molecules containing hydroxyl groups.⁷⁵ Negative charge of GO resulted from ionization of carboxyl groups ($-COOH$)⁷⁶ allows electrostatic interaction with positively charged molecules. The graphitic domains of GO allows π - π interaction with π -conjugated materials.¹⁸ Also, GO can be dispersed in various solvent e.g., water, DMF, DMSO and ethylene glycol, which is due to its amphiphilicity (hydrophilic edges arise from oxygen-containing functional groups and hydrophobic central basal plane originated from the graphitic domains). Therefore, The supramolecular assembly of GO is possible by different non-covalent bonds in various interfaces. Also, many functional groups on GO allow hybridization with a big variety of materials such as DNA, metal oxides, polymers, inorganic nanoparticles and others.⁷⁷⁻⁸⁰

The interaction of GO with other components bound by covalent or supramolecular interaction has been studied by different methods. For example, GO can quench the florescence of several dye-labeled peptides for biosensing⁸¹ or can quench the fluorescent assay of biomolecules such as amino acids and proteins.³² This quenching process is studied by florescence spectroscopy. Another method which has been extensively used to

investigate the aqueous dispersibility of GO at various pH values,⁸² as well as GO's interaction with other charged materials e.g., organic polymers is zeta potential measurement (ζ).²⁹ Zeta potential is an important factor in many applications such as characterization of biomedical polymers,⁸³ electrokinetic transport of particles⁸⁴ or blood cells⁸⁵ and microfluidics.⁸⁶

2.3.2. Method: Zeta potential

The suspension of particles with surface charges exhibits a zeta potential. The surface charges of the particle attract the surrounding counterions, which try to compensate the surface charge. The particle's surrounding containing the counterions, which are influenced by the surface charge of particle is called "electrical double layer". This layer is divided into two separated regions: the stern layer, which is the inner region with ions strongly bounded to the particle and the diffuse layer, which correspond to the outer layer with loosely associated counterions (**Figure 2.1**). The particle and the bounded / associated ions move together due to gravity or due to an applied electrical field. The ions within a certain boundary around the particle move with the particle. This limiting border lies somewhere within diffuse layer and is called "hydrodynamic shear" or "slipping plane" (Figure 2.1). The zeta potential is the potential, which exists at the slipping plane. The particles with large negative / positive zeta potential (± 30 mV) repel each other and therefore the colloidal solution will be stable. The particles with zero surface charge – which could be present at a particular pH, assuming the surface charge is related to proton dissociation – are very unstable and flocculation is very likely. This point of zero charge is related to the isoelectric point, also known from electrophoresis.

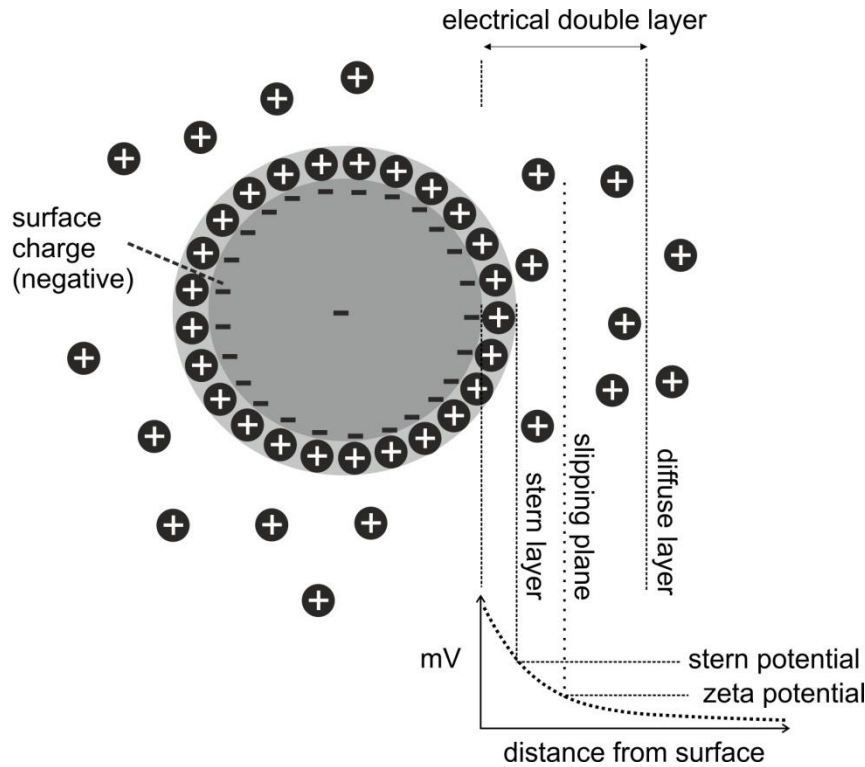


Figure 2.1. Schematic representation of the distribution of cations around a particle with negative surface charge in solution.

In electrophoresis, an electric field is applied across the colloidal solution of the sample, which induces charged particles to move toward the electrode of opposite charge. The direction and velocity of the particles depend on the applied field. The electrophoretic mobility of a particle under the influence of an electric field is defined as the quotient of the velocity of the particle and the electric field strength:

$$\mu_e = \frac{v}{E} \quad \text{Eq. 2.1}$$

where μ_e is electrophoretic mobility, v is particle drift velocity and E is electric field strength. The Zeta potential is not directly measureable. Therefore, there is an approximation that allows calculating the Zeta potential from the electrophoretic mobility, which can be measured by laser-doppler-velocimetry technique. The setup of this technique is shown in **Figure 2.2** and it functions as follows: the emitted beam from the laser is split into two beams by the beam splitter (i). The separated beams are focused by the lens (ii). The beam intersection lies in the solution of charged particles (sample). The crossing beams form an interference pattern with a fringe spacing Λ (Figure 2.2) (iii). An

electrical field is applied through the sample, which causes a flow of the charged particles (iv). While the particles pass through the interference pattern, they scatter the light and thus produce a scattering signal (v) with a shifted frequency compared to the incident beam. The scattered signal is then focused by the second lens (vi) and detected by the detector (vii) (Figure 2.2). The electrophoretic mobility can be calculated from the measured Doppler frequency shift. By application of Smoluchowski theories,⁸⁷ the measured particle mobility can be converted to the Zeta potential as shown in Henry's equation:

$$U_E = \frac{2\varepsilon z f(ka)}{3\eta} \quad \text{Eq. 2.2}$$

where U_E is electrophoretic mobility, z zeta potential, ε dielectric constant, η viscosity and $f(K_a)$ Henry's function ($f(K_a)$ in aqueous solution is often 1.5 and in non-aqueous solution is 1).

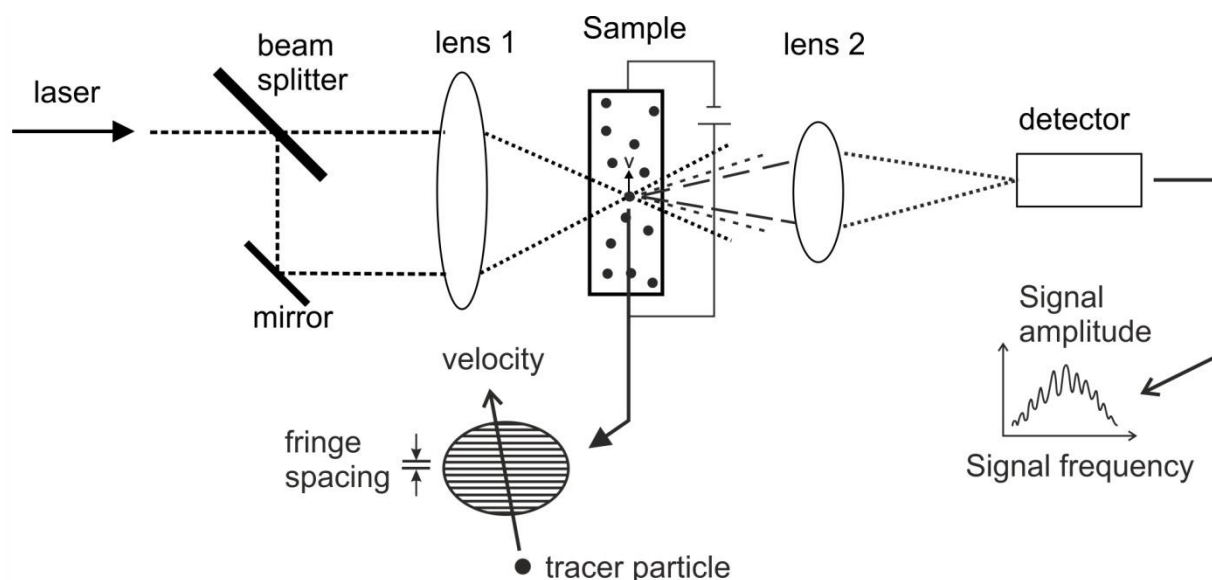


Figure 2.2. Principles of laser Doppler velocimetry.

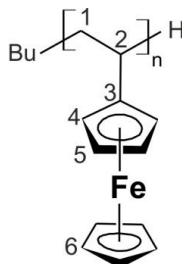
2.3.3. Experimental section

2.3.3.1. Instruments

Vis absorption spectra were measured using a photodiode array agilent 8452 UV-visible spectrophotometer (Hewlett Packard). Zeta potential values were obtained using a Zetasizer nano ZS (Malvern Instruments, Model ZEN3600) at 25°C with a 633nm laser in a DTS1070 cell. The sonification was performed using ultrasonic bath (VWR USC300TH, 80W). AFM images were captured with Flex-Axiom “Nanosurf” using supersharp silicon probe (SSS-NCLR, NANOSENSORSTM) in dry state.

2.3.3.2. Chemicals

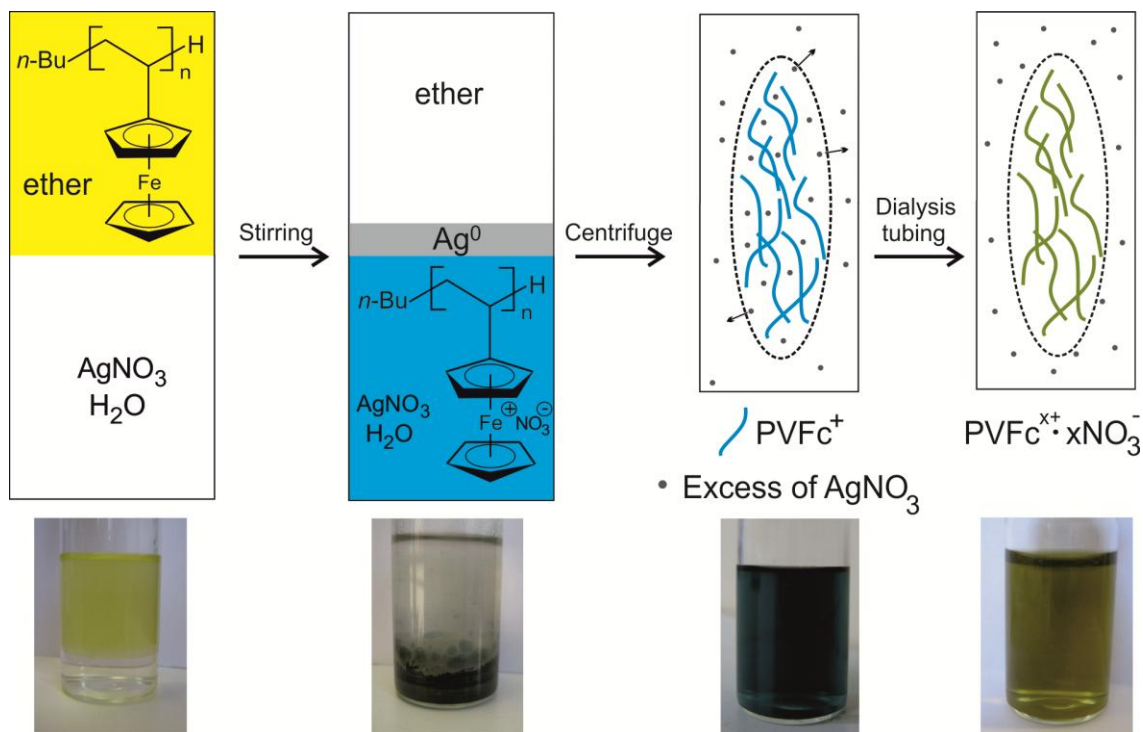
All the chemicals and solvents were from Sigma-Aldrich and used as received without further purification, unless otherwise stated. Solvents for the electrochemistry and spectroscopy were of 99.9% purity. Acetonitrile and diethyl ether were from Sigma Aldrich (> 99.9%). Silver nitrate (AgNO_3) was purchased from Fluka (> 99.0% purity). Graphene oxide (GO) was from “Graphenea” delivered as an aqueous solution (4 mg GO in 1 mL H_2O); elemental analysis: carbon: 49 – 56%, hydrogen: 0 – 1%, nitrogen: 0 – 1%, sulfur: 0 – 2% and, oxygen: 41 – 50%; monolayer content (measured in 0.5 mg/mL): >95%; pH: 2.2 – 2.5. The cellulose membrane for dialysis tubing was from “SPECTRUMLABS” with MWCO: 3.5 kDa. PVFc was delivered with following characteristics: ⁸⁸ size exclusion chromatography (conventional vs PS standards), RI 7070 g/mol, $M_n - M_w$ 8870 g mol⁻¹ and PDI 1.26. SEC-MALLS RI: M_w : 11640 g/mol. ¹H NMR (CDCl_3): δ = 0.80-2.70 ($\text{H}^{1,2}$), 3.65- 4.55 (H^{4-6}). ¹³C NMR (CDCl_3): δ = 33 (C^1), 43 (C^2), 67 ($\text{C}^{4,5}$), 68.5 (C^6), 95.5 (C^3).



The purity of PVFc was further assessed by a Vis absorbance in diethyl ether using ϵ (monomeric ferrocene) = 420 as a standard,⁸⁹ shows 98% of the expected subunits (see Figure 2.3 and subchapter 2.3.3.3 for more details). Additionally, the observed coulombs (integral of cathodic peak) of a thin polymer layer (200 nm) obtained from a cyclic voltammetry test shows > 96% of the applied subunits (see Figure 2.23 and subchapter 2.5.3 for more details).

2.3.3.3. Oxidation of poly(vinylferrocene) (PVFc)

50 mg PVFc (see 2.3.3.2 for details) was dispersed in diethyl ether (300 ml), then 0.1M AgNO₃ (50 ml) was added (**scheme 2.2**). The resulting biphasic solution was agitated by mechanical stirring (1300 rpm) for 50 min. The end of the reaction was indicated by the disappearance of yellow color in the organic phase and appearance of blue color in the aqueous phase. Precipitated Ag⁰ between the two phases was removed by filtration. The blue aqueous phase was isolated and centrifuged to remove remaining silver particles. The excess of AgNO₃ was removed by dialysis tubing of the aqueous phase (extracting compartment: agitated water for four days, daily exchanged). Separation of the phases and dialysis of the aqueous phase - to get rid of excess Ag⁺ ions - yielded a green aqueous solution of partially oxidized PVFc (PVFc^{x+}·xNO₃⁻), which was stable over 8 months (Scheme 2.2).



Scheme 2.2. Two phase oxidation of PVFc by AgNO_3 . Left to right: PVFc in ether and AgNO_3 in H_2O ; upon stirring: oxidized PVFc^+ excess AgNO_3 in H_2O and Ag^0 at the interphase; upon centrifuge: separation from Ag^0 ; upon dialysis tubing: separation from excess AgNO_3 .

The concentration of the solutions used in Vis measurements are the same as explained in the oxidation of PVFc (current subchapter). Analysis of the Vis absorbance using ϵ (monomeric ferrocene) = 420 as a standard⁸⁹ indicates that 95 % of the subunits were oxidized prior to dialysis tubing (**Figure 2.3**). This was shown by development of a peak at 631 nm in the aqueous phase during oxidation, which is characteristic for the ferrocenium ion.⁹⁰

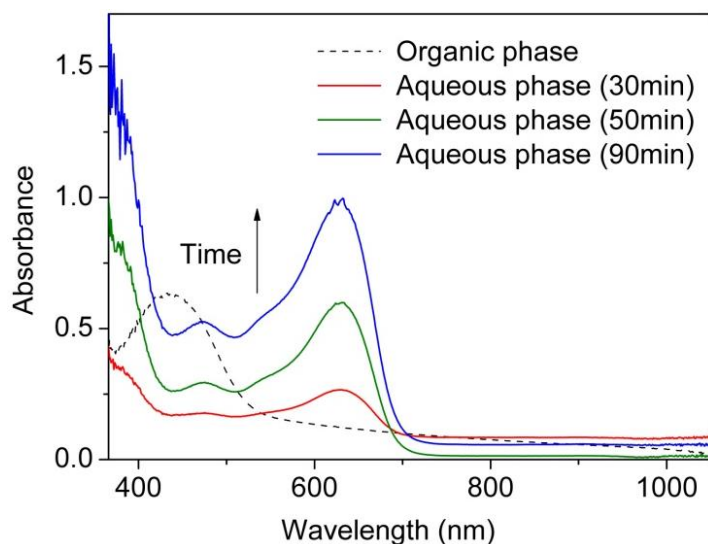


Figure 2.3. Oxidation of PVFc by AgNO_3 as evidenced by Vis analysis. Oxidation was here performed in the biphasic mixture of $\text{CHCl}_3/\text{water}$, as it was slower and easier to follow as compared to the ether / water mixture.

The final solution contains 4.7×10^{-3} M PVFc subunits (only 29 % survived the dialysis, possibly because of the absence of free Ag^+) with NO_3^- counter ions and a small amount ($< \text{ca. } 2 \times 10^{-3}$ M) of a NO_3^- salt formed during dialysis (**Figure 2.4**).

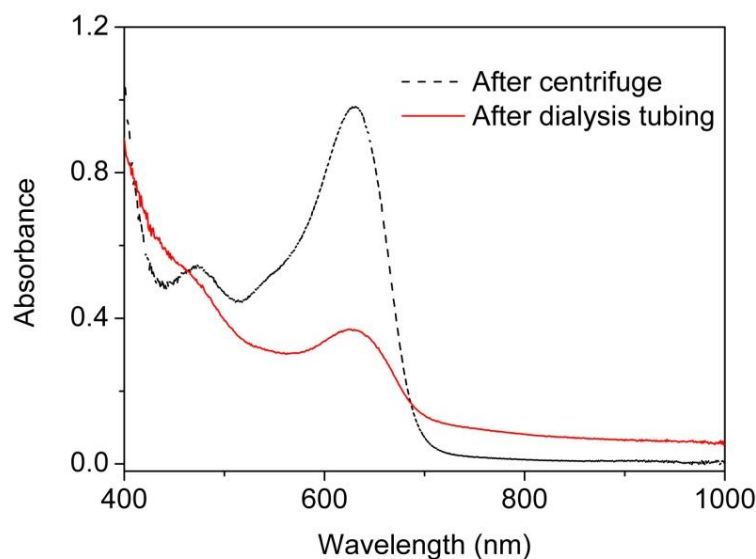


Figure 2.4. Absorption spectra of PVFc^+ after centrifuge in water (dashed black line, oxidized PVFc = 95 %), and after dialysis tubing in water (red line, oxidized PVFc = 29%). The percentage of oxidized ferrocene moieties in PVFc was calculated from the extinction coefficient of ferrocene ($\epsilon=450$).

2.3.3.4. Zeta potential measurements

An aqueous solution of commercial GO (see 2.3.3.2 for details) was diluted to 0.1mg in 2ml H_2O and sonicated for 30 minutes using an ultrasonic bath. Appropriate volumes of the PVFc^{x+} solution (4.7×10^{-3} M, 5 ml, containing 5 mg of PVFc) were added

under sonification over 10 min to 0.1 ml of the GO solution and the final mixtures were diluted to 1ml under sonification for another 5 min. The polymer solutions with same concentration were prepared accordingly. 0.8 ml of the dispersions was measured in a DTS1070 cell (see 2.3.3.1 for details). An average value was calculated from six subsequent measurements.

2.3.3.5. Modeling

The following programs were used: Hyperchem (HyperChem(TM) Professional 8.0.8, Hypercube, Inc., 1115 NW 4th Street, Gainesville, Florida 32601, USA), Arguslab (M. Thompson, ArgusLab 4.0.1, Planaria software LLC, Seattle, Wash, USA, [HTTP://www.arguslab.com](http://www.arguslab.com), 2004), Gabedit 2.4.8⁹¹ and MOPAC (J. Stewart, MOPAC2012, Stewart Computational Chemistry, Colorado Springs, CO, USA, [HTTP://OpenMOPAC.net](http://OpenMOPAC.net), 2012). Modeling was performed by Lorenz Walder.

2.3.3.6. Atomic Force Microscopy (AFM)

The electrodes were prepared by drop casting of GO (ca. 20 $\mu\text{g cm}^{-2}$) or $\text{PVFc}^{\text{x}+} \cdot \text{xNO}_3^-$ (ca. 12 $\mu\text{g cm}^{-2}$) or PVFc@GO solution ($\text{PVFc} / \text{GO} = 1$, ca. 14.7 $\mu\text{g cm}^{-2}$) on the glassy carbon electrode followed by drying at 50°C for 1 hour results in GO@GC or $(\text{PVFc}^{\text{x}+} \cdot \text{xNO}_3^-)\text{@GC}$ or $(\text{PVFc@GO})_n\text{@CC}$, respectively. The AFM images were captured by Shamaila Sadaf.

2.3.4. Results and Discussion

2.3.4.1. Zeta potential measurement

A strong electrostatic interaction and a stable contact between $\text{PVFc}^{\text{x}+} \cdot \text{xNO}_3^-$ and $\text{GO}^{\text{m-}}$ are key factors for producing a composite, in which GO is homogenously distributed in the polymer matrix. The quality of the PVFc@GO dispersion is crucial for

high capacity and fast kinetics (fast electron and ion flow) in the final battery material PVFc@rGO assuming pre-organization takes place mainly in the presence of GO but not with rGO.⁹² In addition, the real capacity and energy densities depend on the ratio of redox active polymer to conductive filler - a fact that is often neglected in literature.⁶⁶ Zeta potential measurements can be used to study dispersions with variable surface charges, such as expected in the case of $\text{GO}^{\text{m-}}$ in the presence of different amounts of $\text{PVFc}^{\text{x+}}$, and to evaluate the stability of the resulting complexes dispersion.⁹³ In the current study, the method was used to optimize the $\text{PVFc}^{\text{x+}} / \text{GO}^{\text{m-}}$ weight ratio with respect to (i) colloidal stability, and (ii) with respect to tight contact between $\text{GO}^{\text{m-}}$ and all $\text{PVFc}^{\text{x+}}$ strands, i.e. to find the highest possible $\text{PVFc}^{\text{x+}} / \text{GO}^{\text{m-}}$ weight ratio with all $\text{PVFc}^{\text{x+}}$ strands bound. The zeta potential value of pure $\text{GO}^{\text{m-}}$ in the aqueous solution was -36.9 mV, as reported, due to dissociated carboxylic acids (**Figure 2.5**).⁹⁴ The pure $\text{PVFc}^{\text{x+}} \cdot \text{xNO}_3^-$ solution with ca. 29% oxidized sites shows increasing Zeta potential values from $+2$ and $+38$ for increasing polymer concentration probably due to aggregating of PVFc at higher concentrations. The addition of $\text{PVFc}^{\text{x+}} \cdot \text{xNO}_3^-$ to an un-buffered aqueous $\text{GO}^{\text{m-}}$ solution shows that the zeta potential describes a sigmoidal shape with increasing weight ratio of $\text{PVFc}^{\text{x+}}$ to $\text{GO}^{\text{m-}}$ demonstrating the incremental coverage of $\text{GO}^{\text{m-}}$ with $\text{PVFc}^{\text{x+}}$ (Figure 2.5). Interestingly, deviation of the original surface charge of $\text{GO}^{\text{m-}}$ starts only at weight ratios larger than 1 ($\log \text{ratio} > 0$) with an isoelectrical point at $\text{ratio} \sim 2.7$ and continuing into positive zeta potentials up to a weight ratio of ca. 10. This indicates that very heavy loading of single GO sheets with $\text{PVFc}^{\text{x+}}$ of up to 10 times the weight of underlying $\text{GO}^{\text{m-}}$ is possible, and that these colloidal particles are still intact. At even higher weight ratios (above $\log 10$) the zeta potential flattens and values observed for the pure polymer indicating the presence of free polymers beside the heavily loaded GO sheets. Notably, the zeta potential was measured in an experiment based on light scattering, which is restricted to molecular size > 10 nm.

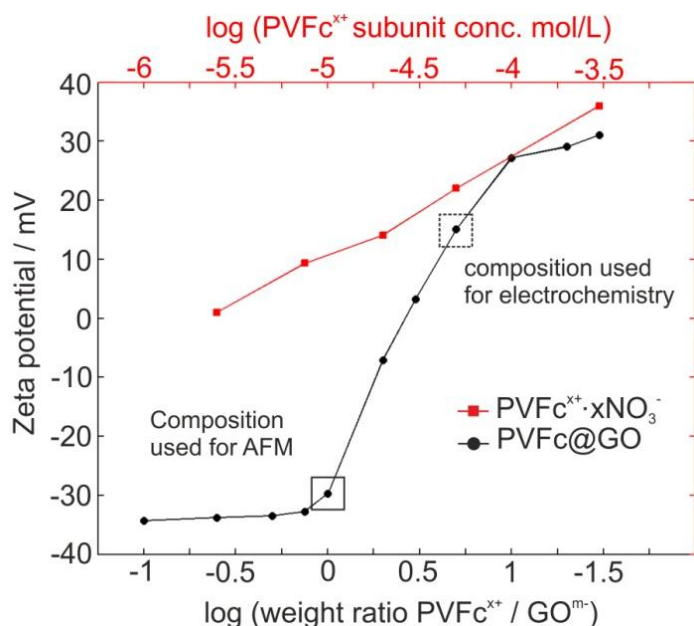


Figure 2.5. Zeta potential of GO^{m-} (0.05 w%, -36.9 mV) in the presence of increasing amounts of $PVFc^{x+} \cdot xNO_3^-$ given as log (weight ratio) (-●- black); and zeta potential of $PVFc^{x+} \cdot xNO_3^-$ at different subunit concentrations (-■- red). Notably, the $PVFc^{x+} \cdot xNO_3^-$ concentration axis is valid for both curves. Preparation of the solutions is explained in the subchapter 2.3.3.4.

As known from literature, I also found stable colloidal solutions (stability > 8 months) for $|Zeta\ potential| > 30\ mV$ (**Figure 2.6**), but relatively unstable colloidal solutions (stability < 3 days) for $|Zeta\ potential| < 10\ mV$.⁹⁵

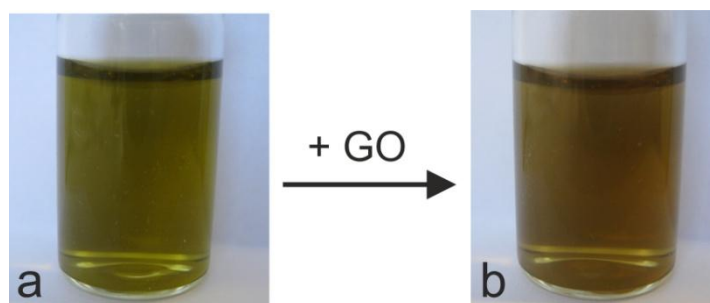


Figure 2.6. Colloidal stability of $PVFc^{x+} \cdot xNO_3^-$ and $PVFc@GO$. $PVFc^{x+} \cdot xNO_3^-$ (a) and $PVFc@GO$ (b) with a weight ratio of 4.4/1($PVFc^{x+} / GO^{m-}$) in H_2O . Both solutions were stable for at least 5 months. Preparation of the solutions is explained in the subchapter 2.4.2.3 - a.

2.3.4.2. UV-Vis measurement

The electrostatic interaction of GO^{m-} and $PVFc^{x+} \cdot xNO_3^-$ was further confirmed by Vis measurements (**Figure 2.7**). Vis spectra of $PVFc^{x+} \cdot xNO_3^-$ after dialysis in the presence of decreasing weight ratio $PVFc^{x+} / GO^{m-}$, 1) 100/1, 2) 18/1, 3) 13/1, 4) 8/1. The pure $PVFc^{x+} \cdot xNO_3^-$ exhibits a peak at 630 nm that is attributed to the ferrocenium ion.

Step wise addition of GO to partially oxidized PVFc resulted in a decrease of the absorbance of the ferrocenium ion concentration (factor: 0.57). This, points to the formation of a charge transfer complex and / or charge injection from $\text{GO}^{\text{m-}}$ into $\text{PVFc}^{\text{x+}}$, a phenomenon known from literature.⁹⁶

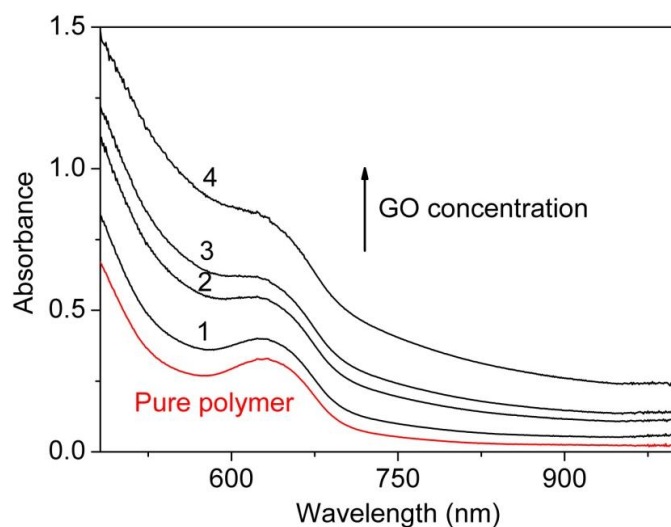


Figure 2.7. Loss of oxidized $\text{PVFc}^{\text{x+}} \cdot \text{xNO}_3^-$ upon interaction with GO. The dilution effect was corrected. $\text{PVFc}^{\text{x+}}$ concentration was $4.7 \times 10^{-3} \text{ M}$ and a 0.5 mg / ml GO solution was used (see 2.3.3.3 and Figure 2.4 for experimental details).

2.3.4.3. Molecular modeling

A model study based on the size and specific weight of PVFc indicates multi layers of tightly packed PVFc strands deposited between single GO sheets even at $\text{PVFc}^{\text{x+}} / \text{GO}^{\text{m-}}$ weight ratio as low as 1:1 (**Figure 2.8**). A neutral 16mer of PVFc ($\text{C}_{191}\text{H}_{190}\text{Fe}_{16}$ (one $-\text{CH}_2-$ group is cut off) was prepared using the graphical editor in Hyperchem, then imported into GABEDIT⁹¹ and geometry optimized "in acetonitrile" using the semiempirical method PM7 in MOPAC12. The PM7 keywords included a correction for the size and dielectric constant of acetonitrile. The resulting structures were generally cylindrical with some curvature, but many local minima with different extend of curvature were found. Partially oxidized 16mer (2+, 4+ and 6+) with and without counter ions were also calculated, but they showed almost the same size and shape except slightly less curvature. A simplified graphene oxide sheet ($\text{C}_{130}\text{O}_{54}\text{H}_{48}^{-6}$, 35% oxygen content) was prepared from graphene containing 158 sp^2 carbons by addition of 54 water molecules

over C,C-double bonds from both sides of the graphene plane (6 of them deprotonated at O) using the editor of Arguslab . The GO sheet is puckered after a few cycles of UFF optimization due to the C sp³ centers and due to the mutual repulsion of the 6 neg. charges. The oxygen weight content of C₁₃₀O₅₄H₄₈⁻⁶ (without consideration of small counter ions) is 100*Mw_O / Mw_{GO} = 100*864 / 2472 = 35%, i.e., in the range of the specification of the product (*see 2.3.3.2 for details*). The x-y size of the average plane of the graphene oxide sheet C₁₃₀O₅₄H₄₈⁻⁶, 22.5 * 14.1 Å) is similar to the size of the plane of the parent graphene sheet (22.0 * 14.2 Å), because -OH groups are occupying space below and above the plane, and because sp³-puckering is counterbalanced by longer C,C bond lengths, and because the carbon skeleton is not interrupted.

The 16mer PVFc from PM7 optimization (see Figure 2.9 - d) can be described by a cylinder with length L_{16m3er} = 3.4 nm and circle area A_{16m3er} = 2.0 nm² leading to the

$$\text{volume } V_{16\text{mer}} = 6.8 \text{ nm}^3$$

$$\text{projected area of cylinder along the short axis, } PA_{16\text{mer}} = 1.6 * 3.4 = 5.4 \text{ nm}^2$$

$$\text{cylinder mass} = M_{16\text{mer}} : (16 * C_{12}H_{12}Fe) - (CH_2) = C_{191}H_{190}Fe_{16} = M_{16\text{mer}} = 3380 \text{ g/mol}$$

packed PVFc cylinders on GO: arial mass density_{PVFc} =

$$3379.6 \text{ g} / 5.4 \text{ mol nm}^2 = 626 \text{ g/mol nm}^2$$

$$\text{corresponding GO plane: } 2473 / (1.2 * 2.3) = 2473 / 2.8 = 883 \text{ g/mol nm}^2$$

$$\text{Mass ratio for a single layer of packed cylinders of PVFc on GO is: } = 0.707$$

$$\text{number of packed single layers at mass ratio 1.0: } = 1.41$$

$$\text{number of packed single layers at zeta potential 0 with mass ratio 2.7: } = 3.8$$

$$\text{number of packed single layers at mass ratio 4.4 (used for battery material) } = 6.2$$

According to the above calculations, it is clear that a single layer of tightly packed cylindrical polymer molecules on a GO sheet can only account for a mass ratio PVFc / GO = 0.707. The Zeta-potential = 0 is achieved for PVFc / GO = 2.70 meaning that in the average 3.8 layers of tightly packed PVFc cylinders are necessary per GO

sheet, and that at the ratio PVFc / GO = 4.40 even 6.2 tightly packed layers are necessary. Notably, it is assumed that the slipping plane limit in pure GO, pure polymer and PVFc@GO are similar and can therefore be neglected (see subchapter 2.3.2).

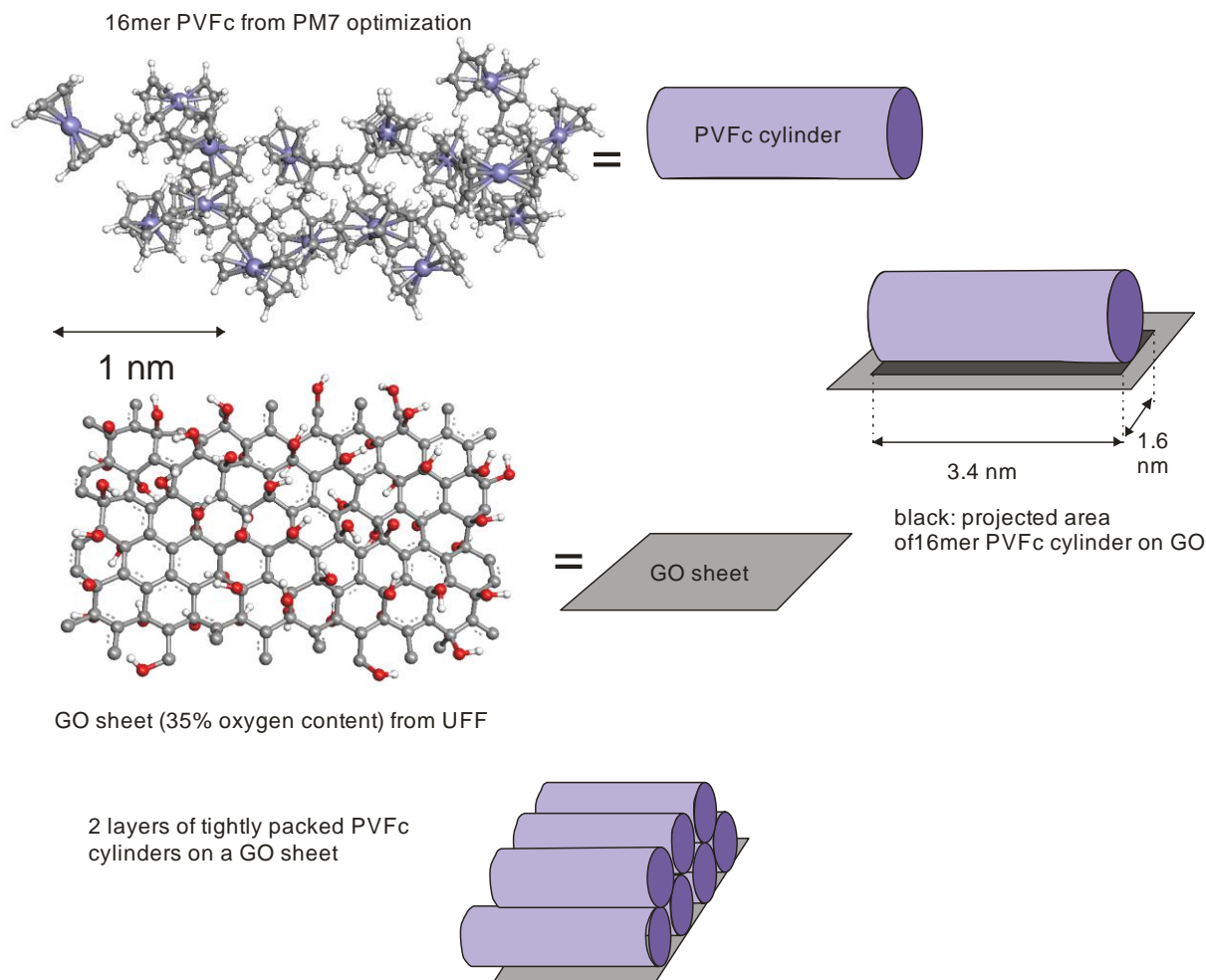


Figure 2.8. Molecular modeling of surface coverage of GO sheets with PVFc strands. The programs used for modeling is listed in 2.3.3.5.

2.3.4.4. Morphology of PVFc@GO complex in dry state

For atomic force microscopy (AFM) measurements, thinner films with a composition indicated by the plane square in Figure 2.5 (zeta potential = -30, weight ratio = 1) was used (in order not to cover all structural features of (PVFc@GO)@GC with PVFc). The AFM images are shown in **Figure 2.9**. Pure GO@GC (a and a') shows long

range architectures of folded / wrinkled GO platelets / GO sheets with distinct folds over several μm (broken curve), extended surfaces (broken line square) and > 50 nm deep holes / tunnels (broken circle). Pure $(\text{PVFc}^{\text{x}+} \cdot \text{xNO}_3^-)@\text{GC}$ (b and b') consisting of 57 PVFc subunits shows overlaid oval shapes with smallest resolvable lengths of ca. 60×40 nm (limit of lateral resolution of the AFM tip, broken square) and smallest heights of 2-3 nm. Semiempirical PM7 geometry optimization predicts a curved cylindrical shape for a hexadecameric PVFc with 1.6 nm diameter and 3.4 nm length, i.e., a length of 12 nm for the polymer in use with 57 average subunits (see d in Figure 2.9). Some tendency for chain formation of the globuli by lateral stacking (broken curves without principal direction) was observed, however XRD measurement did not show any crystallinity. Furthermore, the formation of tunnels by circular / cylindrical aggregation of the globuli (broken circles) is observed. Most interesting is the AFM of $(\text{PVFc}@\text{GO})@\text{GC}$ (c,c' in Figure 2.9). The low weight ratio of 1 used for the composite preparation allows to see some features of the specific interaction. Most obvious is a principal direction of the PVFc globuli over several μm (c, broken arrows). Such parallel long range arrangement is not observed in the AFM image of the pure polymer without GO, nor with GO without PVFc. These lines are interpreted as a result of PVFc decorated GO sheets, which have been flattened and parallel stacked during the process of complex formation and drying, respectively. In addition, cylindrical mesopores are again observed (broken circles). In conclusion, the AFM images indicate an ion percolating structure, which may also become electron percolating after GO / rGO transformation.

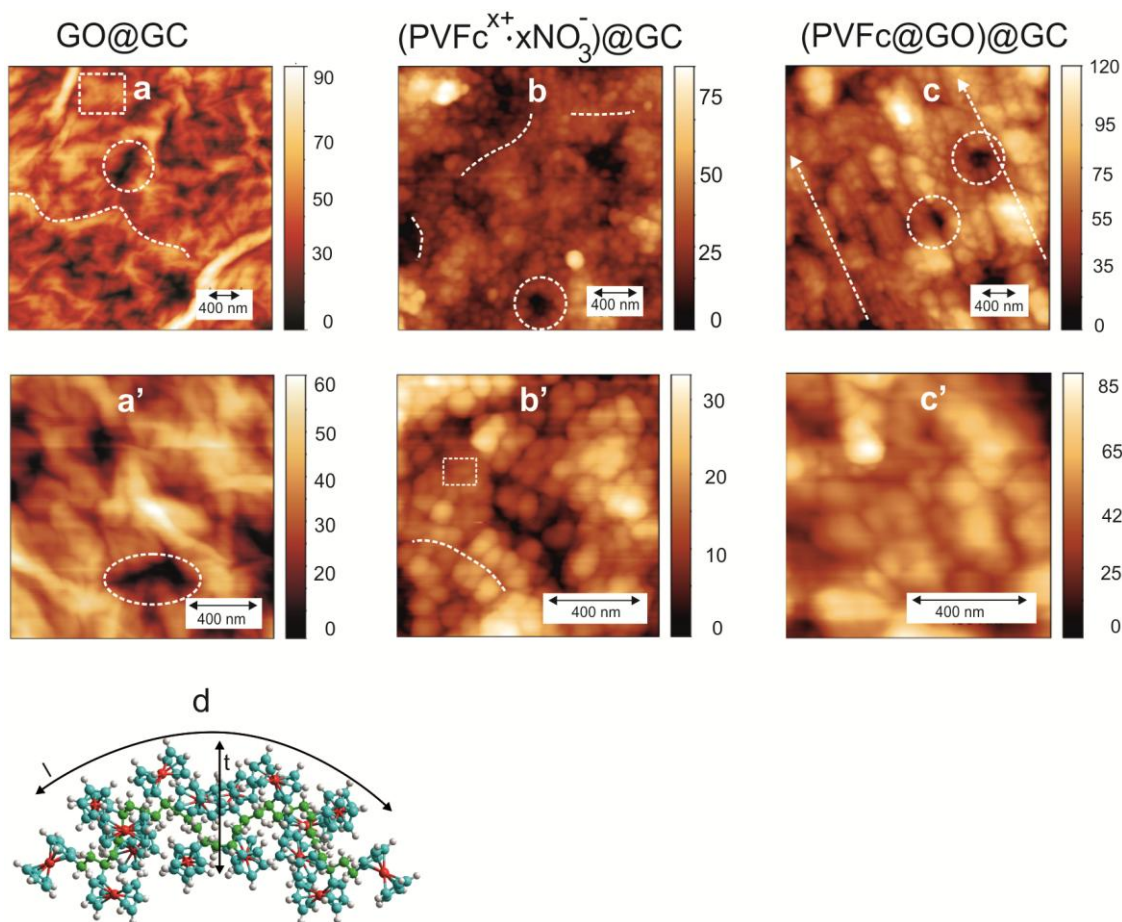


Figure 2.9. AFM images of ca. 500nm thick layers of ca. $20 \mu\text{g cm}^{-2}$ GO@GC (a, a'), of $\sim 12 \mu\text{g cm}^{-2}$ $(\text{PVFc}^{x+} \cdot x\text{NO}_3^-)\text{@GC}$ (b, b') and of ca. $14.7 \mu\text{g cm}^{-2}$ $(\text{PVFc@GO})\text{@GC}$ (mass ratio $\text{PVFc}^{x+} / \text{GO}^{m-} = 1$) (c, c'), scan lengths: ca. $3 \mu\text{m}$ (a-c) and ca. $1 \mu\text{m}$ (a'-c'); pure GO@GC (a and a'): long range architectures of folded/wrinkled GO platelets/GO sheets with distinct folds over several μm (broken curve), extended surfaces (broken line square) and $>50 \text{ nm}$ deep holes/tunnels (broken circle); pure $(\text{PVFc}^{x+} \cdot x\text{NO}_3^-)\text{@GC}$ (b and b', average PVFc subunits: 57): smallest resolvable lengths of ca. $60 \times 40 \text{ nm}$ (broken square, limit of lateral resolution of the AFM tip, broken square) and smallest heights of 2-3 nm; chain formation of the globuli by (broken curves) and tunnels from circular/cylindrical aggregation of the globuli (broken circles); $(\text{PVFc@GO})\text{@GC}$ (c,c') with principal direction of the PVFc globuli (c), (broken arrows) and cylindrical mesopores (broken circles); d) PM7-optimized structure of an uncharged 16mer PVFc oligomer (green atoms: backbone carbons) showing a thickness (t) of ca. 1.6 nm and a length (l) of ca. 3.4 nm. The details on electrode preparation and instrument exhibited in 2.3.3.6 and 2.3.3.1, respectively.

2.3.5. Summary

In the subchapter 2.3, the electrostatic interaction of GO and partially oxidized PVFc in the solution and the morphology of the GO@GC, $\text{PVFc}^{x+} \cdot x\text{NO}_3^- \text{@GC}$ and $(\text{PVFc@GO})\text{@GC}$ in dry state were studied. Zeta potential measurement have shown that

the negative surface charge of GO, along addition of PVFc^{x+}, turned to positive, which shows the surface coverage of GO by the cationic polymer. This electrostatic interaction was further evidenced by Vis measurement, which showed formation of a charge transfer complex and / or charge injection from GO^{m-} into PVFc^{x+}. Modeling showed that at the stable colloidal regions (zeta potential > 15 mV), multilayer of PVFc are surrounding the GO sheets. Therefore, in the PVFc / GO = 4.4, which was used for battery application, polymers are in direct / close contact to GO sheets, which is very important for high rate devices. AFM images showed that each of GO alone and polymer alone construct hole / tunnels upon film formation. However, AFM images of composite showed long range arrangement of PVFc strands – which was not observed in the polymer alone – that are probably polymers patterned by GO sheets. Furthermore, the composite material has cylindrical mesopores, which can provide an excellent ion percolating system.

2.4. Electrocatalytic transformation of (PVFc@GO)_n@CC to (PVFc@rGO)_n@CC by viologen

2.4.1. Introduction

The supramolecular formation of graphene oxide and PVFc^{x+} was shown in the previous subchapter (2.3). However, due to the lack of conductivity in this composite, a GO/rGO transformation step prior to battery tests is necessary. Thus, in this subchapter a method to transform the non-conductive GO-polymer to conductive rGO-polymer will be described.

Graphene possesses unique electrical and mechanical properties, which make it an ideal candidate for many energy-related applications such as batteries, supercapacitors, solar cells and etc.^{6, 18, 22-25} Therefore, there have been many methods suggested to synthesize graphene e.g., chemical vapor deposition (CDV), plasma enhanced CDV, electric arc discharge and others.⁹⁷⁻⁹⁹ However, considering mass production and synthesis cost, the oxidation of graphite to graphite oxide, its conversion to graphene oxide (GO) and the subsequent reduction of GO is the most promising method.⁶⁷ Notably, this method is compatible with the intermediate PVFc@GO composite described in the previous subchapter.

Based on different models proposed for the molecular structure of GO such as Hoffmann, Ruess, Nakajima–Matsuo, and Lerf–Klinowski, a sheet of GO possesses many oxygen-containing functional groups such as carboxyl, hydroxyl, epoxy and keto on the basal planes and the edge of the sheets.^{63-64, 100} During graphite / GO transition, the conjugating domains of graphite bearing sp² carbons are converted to the non-conjugated sp³ carbons. As a result, the electronic conjugation of the graphite is disturbed in GO. Reduction of GO regenerates the electronic conjugation in reduced graphene oxide (rGO) and therefore conductivity is reestablished. The electronic conductivity of rGO is 200-2400 S m⁻¹ (depending on the reduction method),¹⁰¹⁻¹⁰² which is comparable with pure graphite 2500 ± 15 S m⁻¹.¹⁰³

Chemical-, thermal- and electrochemical-reduction are the most promising methods reported to reduce GO. Chemical methods use reducing agents e.g., hydrazine and hydroquinone.³⁴ The reduction quality is very promising, however, hydrazine is hazardous and may damage the environment. GO reduction by metals e.g., Fe, Al and Zn has also attracted much attention, but remaining metal impurities are a big drawback.¹⁰⁴⁻¹⁰⁶ Thermal reduction can efficiently remove the oxygen-containing functional groups of GO, however, GO reduction by this method needs high temperatures ($> 600^{\circ}\text{C}$).³⁵ For the case of GO composites with organic polymers, the possible instability of the polymer material at such temperatures makes this method less general. The electrochemical reduction of GO is green (no toxic solvents / additive are used), fast and the synthesized rGO is contaminant free.¹⁰⁷⁻¹⁰⁸ Moreover, the electrical conductivity and electrochemical stability of rGO synthesized by the electrochemical method are higher than for previous methods. This is probably due to the small residual defects remaining after chemical and thermal reduction.⁶⁷ The electrochemical reduction process is very simple, i.e., application of a cathodic potential (-1.5 V vs. SCE) to the GO electrode in an acidic environment, however, the exact mechanism is still unclear. In spite of the mentioned advantages of the electrochemical method, the reduction of the electrodes with thick layers of GO is very slow and inefficient.

2.4.2. Experimental section

2.4.2.1. Instruments

Cyclic voltammetry analyses using Autolab potentiostat (PGSTAT 20) interfaced to a computer with the GPS software (version 4.9). The EQCM experiments were conducted in a three-electrode cell from ALS Co., Ltd, Japan (EQCM Flow cell kit) under potential scanning condition using a 5 MHz quartz crystal resonator metalized with gold electrodes. The potential was controlled by a potentiostat (Gamry, Interface 1000) and a frequency analyzer (Gamry, EQCM 10M). Conductivity was measured with an Interdigitated Microsensor Electrode (IME) from “ABTECH Scientific, Inc.” with 50

digit pairs (IME 1525.3-M-Au-U) (surface 0.15×0.3 cm).¹⁰⁹ Raman spectra were recorded with the confocal Raman spectrometer LabRAM HR Evolution equipped with a second harmonic 532 nm Nd-YAG laser for excitation and the duoscan option. Thermogravimetric analysis was performed on a Netzsch STA 449 C at a heating rate of 10°C min⁻¹ in the range of 25 to 550 °C under nitrogen flow. AFM images were captured with Flex-Axiom “Nanosurf.

2.4.2.2. Chemicals

All the chemicals and solvents were from Sigma-Aldrich and used as received without further purification, unless otherwise stated. Solvents for the electrochemistry and spectroscopy were of 99.9% purity. Lithium perchlorate from Sigma (99.99% purity). Methyl viologen dichloride hydrate from Sigma – Aldrich (>98% purity). PVFc and GO as described in the subchapter 2.3.3.2. Oxo-G was synthesized according to the previously described method.¹¹⁰ Flakes of oxo-G have an average density of lattice defects of about 0.5%-0.8% with rather large flake size of 1-10 micrometer and dispersion with a flake size smaller than 1 micrometer.¹¹¹

2.4.2.3. Preparation of PVFc@GO solutions with varying $PVFc^{x+} / GO^{m-}$ ratio

An aqueous solution of commercial GO was diluted to 1 mg / 2 ml and sonicated for 30 minutes using an ultrasonic bath. a) *Weight ratio 4.4:1 $PVFc^{x+} / GO^{m-}$* : the GO solution (2.27 ml, containing 1.14 mg GO) was drop wise added to the $PVFc^{x+} \cdot nNO_3^-$ solution (5 ml, containing 5 mg of PVFc) under sonification over 10 min. Then, 2.73 ml distilled water was added (increasing the volume to 10 ml) and the sonification was continued for another 30 minutes. b) *other $PVFc^{x+} / GO^{m-}$ ratios*: the same procedure as in a) using the same amount of polymer solution, but varying the amount of GO solution for the desired ratio and adjusting the water addition for a final 10 ml volume.

2.4.2.4. Electrochemical measurements and electrode preparation

The electrochemical reduction of the composite was performed in the surface confined state on a glassy carbon (GC) electrode (surface: 0.071 cm², Metrohm, 6.0804.010) or on a 0.5 inch quartz crystal resonators (surface: 0.28 cm² gold electrodes, KVG Quartz Crystal Technology GmbH) or on FTO or ITO (active surface: ca. 1 cm², “Aldrich”). GC was polished with alumina powder, then rinsed thoroughly with water, and dried in the oven at 50°C. The electrodes were prepared by drop casting of a PVFc@GO solution (“a” and “b” in 2.4.2.3) on the current collector followed by drying at 50°C for one hour resulting in (PVFc@GO)_n@CC, with n = 1 meaning 1.68 µl of solution (0.84 µg PVFc^{x+} and 0.19 µg GO). In the case of layers with n > 4, bigger drops in the range between 5-20 µl were also used.

2.4.2.5. Electrochemical transformation of (PVFc@GO)_n@CC to (PVFc@rGO)_n@CC

In all of the electrochemical reduction experiments an aqueous solution of 0.1 M LiClO₄ / 4 mM methyl viologen dichloride (MV⁺⁺) was used as the electrolyte / electrocatalyst. After reduction, the (PVFc@rGO)_n@CC electrode was washed in distilled water to remove all MV⁺⁺ and dried at 50°C for 30 min.

2.4.2.6. Electrochemical Quartz Crystal Microbalance (EQCM):

EQCM is an acoustic sensing method, which functions based on the inverse piezoelectric effect measuring the mass adsorption or the fluid viscosity of the surrounding media. The mass change due to film deposition, GO / rGO transition and composite “breathing” on the gold surface of oscillating quartz crystal causes a change in the resonance frequency as described by the Sauerbrey equation:

$$\Delta f = -C_f m \quad \text{Eq. 2.3}$$

where Δf is the change of the frequency in Hz, C_f is the calibration constant (the calibration constant for a 5 MHz At-cut quartz crystal in air is $56.6 \text{ Hz } \mu\text{g}^{-1} \text{ cm}^2$), and m is the mass change (g cm^{-2}). This technique is very sensitive to small mass changes ($< 0.4 \text{ ng cm}^{-2}$ for a 5 MHz quartz crystal). Electrodes were prepared as described in section 2.4.2.4 i.e., $(\text{PVFc@GO})_{14}\text{@Au}$ (mass density $51.5 \text{ } \mu\text{g cm}^{-2}$) and the electrolyte is $0.1 \text{ M LiClO}_4 / \text{H}_2\text{O} + 4 \text{ mM MV}^{++}$ at $v = 20 \text{ mV s}^{-1}$.

2.4.2.7. Conductivity

A droplet of $(\text{PVFc@GO})_{0.5}$ ($\text{PVFc}^{x+} / \text{GO}^{m-} = 4.4$) was drop casted on the interdigitated electrode region and dried at 50°C for one hour yielding $(\text{PVFc@GO})_{0.5}\text{@IME}$. Both electrodes of the interdigitated sensor were parallel connected and polarized for 20 s at -1.2 V under electrocatalytic conditions, as described for the preparation of electrodes for battery tests (2.4.2.4 and 2.4.2.5) to yield $(\text{PVFc@rGO})_{0.5}\text{@IME}$. After drying, the specific conductivity of $(\text{PVFc@rGO})_{0.5}\text{@IME} = 7.2 \times 10^{-4} \text{ S cm}^{-1}$ was determined from the measured resistance ($180 \text{ } \Omega$), after correction for the active surface (0.045 cm^2), and use of the Zaretsky cell constant (0.13 cm^{-1}) of the sensor.¹⁰⁹

2.4.2.8. Raman spectroscopy

The laser power was set to 0.5 mW and focused by a $50\times$ objective with $\text{NA} = 0.8$. The duoscan option was used to collect average spectra of oxo-G and reduced oxo-G in a spectra range of $3000\text{--}3400 \text{ cm}^{-1}$ using a 600 line / mm grid. The acquisition time was about 30 min per spectrum. Raman spectra were obtained from an area of $20 \times 20 \text{ } \mu\text{m}$ at a laser power of 0.5 mW (532 nm) with an accumulation time of 30 min. The Raman spectra of rGO from MV electrocatalyzed reduction are average spectra. They relate, according to the model introduced in the literature,¹¹²⁻¹¹⁴ to a distance of defects of roughly 2.5 nm , which correlates to a density of defects of 0.5% , taking the lattice

constant of graphene into account. Synthesis and Raman spectroscopy measurements of Oxo-G were performed by *Siegfried Eigler*, and *Christian E. Halbig*.

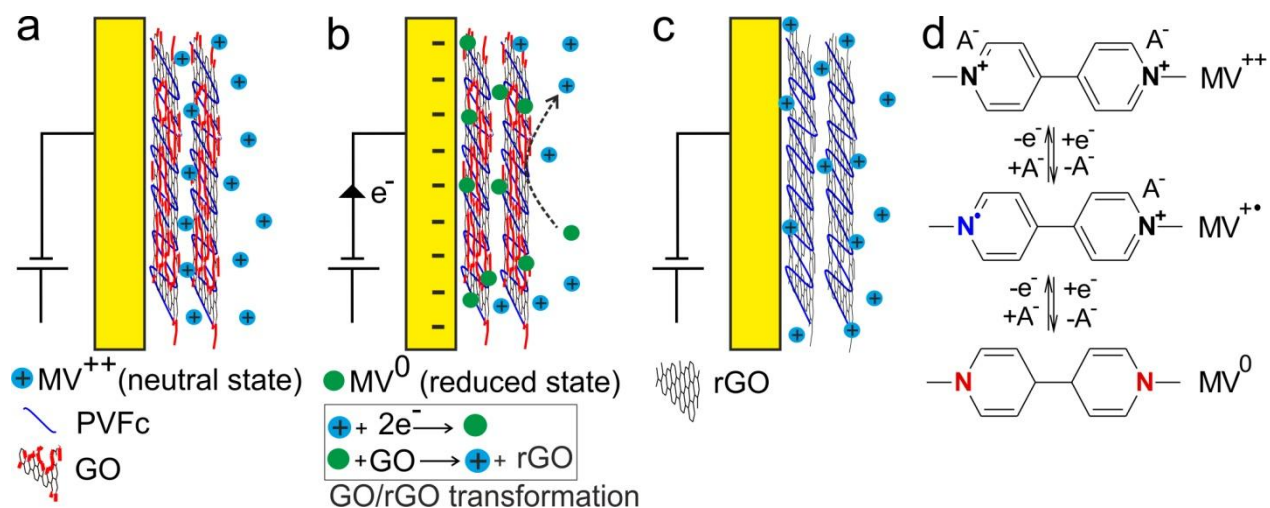
2.4.2.9. Electrochemical AFM

AFM images were captured with Flex-Axiom “Nanosurf” using PointProbe® Plus contact Mode Short Cantilever -Au Coating probe (PPP-NCSTAuD NANOSENSORSTM) for EC-AFM on the Electrochemistry Stage ECS 204 in aqueous 0.1 M KCl (including 4mM MV^{++} for the GO-rGO transition). The potential of the modified GC electrode was stepped vs. a Ag/AgCl reference using a Pt wire counter electrode and a potentiostat (Gamry, Interface 1000).

2.4.3. Results and Discussion

Unlike graphite, GO is electronically insulating and has to be transformed into conductive rGO.¹¹⁵ Among the well-known methods of GO reduction such as chemical, thermal and electrochemical, the latter is faster and the toxic solvents can be replaced by water.^{107, 116} It has been demonstrated that the oxygen-containing functional groups of GO can be reductively eliminated under acidic conditions (pH = 5) by applying a negative potential of -1.5 V (vs. SCE).^{107,116} The electrochemical reduction yields highly conductive rGO but the reduction process of thick layers are slow.^{108,116} In the present study, the same sluggish GO / rGO transformation for (PVFc@GO)@GC was observed, which was essentially even slower than in the absence of PVFc. This is possibly due to the insulating polymers, which segregate GO sheets. Therefore a new electrocatalytic method for the GO / rGO transformation using methyl viologen dichloride (MV^{++}) as an electrocatalyst dissolved in the electrolyte solution is developed. This method shows fast and efficient GO / rGO transformation in a lower potential (smaller than -1V vs. SCE), which is applicable even in the thick layers (> 30 μ m). The idea is based on reports claiming that reduced viologen can transfer electrons to GO sheets and that 4-

cyanopyridinium is able to reduce GO upon reductive dimerization.⁶⁸⁻⁶⁹ Anyhow, there are no reports on the deliberate use of MV^{++} additions to the solution for the electrocatalytic reduction of GO composites at an electrode. A general overview of the GO reduction procedure is shown in **Scheme 2.3**. (PVFc@GO)@CC as the working electrode is immersed in the electrolyte solution, which consist MV^{++} and supporting salts (Scheme 2.3a). Upon applying cathodic potential (< -0.4 V vs. Ag/AgCl), the MV^{++} molecules diffuse into the composite layer and reduce at the surface of CC ($MV^{++} \rightarrow MV^{+\bullet} \rightarrow MV^0$) (Scheme 2.3d). The reduced MV molecules transfer electrons to the GO sheets and in this manner catalyze its transformation to rGO (Scheme 2.3b-c).

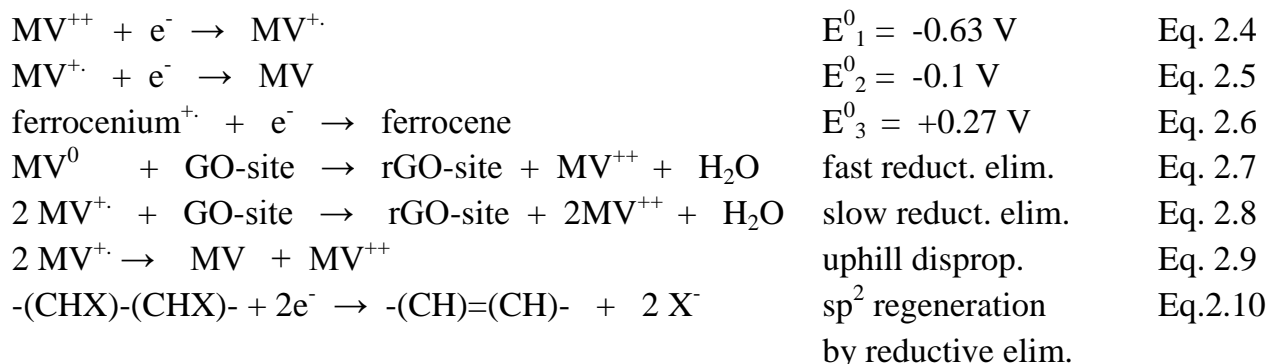


Scheme 2.3. The electrocatalytic transformation of $(PVFc@GO)@CC$ to $(PVFc@rGO)@CC$. CC: current collector (yellow plates); PVFc: poly(vinylferrocene) (blue curves); GO: graphene oxide (black/red sheets); MV^{++} : methyl viologen in the oxidized state (light blue circles); MV^0 : methyl viologen in the reduced state (green circles); rGO: reduced graphene oxide (black sheets). **a**) $(PVFc@GO)@CC$ as the working electrode and MV^{++} + supporting salt dissolved in water as the electrolyte solution (supporting salt is not shown); **b**) cathodic potential is applied: $MV^{++} \rightarrow MV^0$, catalytic reduction of GO; **c**) working electrode i.e., $(PVFc@rGO)@CC$ after GO/rGO transition; **d**) redox states of methyl viologen i.e., MV^{++} , $MV^{+•}$ and MV^0 .

2.4.3.1. Cyclic voltammetry

The reduction mechanism is studied in detail by cyclic voltammetry (CV) measurements. As it was mentioned, MV^{++} is reduced in two stages from the dication via the monocation radical to the neutral species in water (**Eq. 2.4**, **Eq. 2.5** and Scheme 2.3d). As depicted in the overview (Scheme 2.1), electrocatalysis occurs from the singly and the doubly reduced state of MV^{++} . This can be deduced from the cyclic voltammogram (**Figure 2.10**). The electrode has a 14 fold drop-casted / dried $PVFc@GO$ layer on a gold substrate, i.e. $(PVFc@GO)_{14}@Au$. The electrode potential is scanned in water containing 0.1 M $LiClO_4$ / 4 mM MV^{++} for 6 consecutive scans ($0 \rightarrow 0.8 \rightarrow -1.3 \rightarrow 0V$). In the first scan (red line, arrow head indicating scan direction) a weak quasi-reversible wave related to the ferrocene / ferrocenium couple is observed. In the negative potential range the two viologen waves with a large cathodic electrocatalytic contribution are observed. The plateau current is typical for an electrocatalytic situation. The sharp peaks on the viologen reduction are indicative for electrodeposition of reduced viologen.

The second and later scans differ largely from the first one but they are very similar to each other. The electrocatalytic waves are interpreted by the sequence of **Equations 2.4, 2.5, 2.7, and 2.8**:



Other sequences may also be active, e.g. **2.4, 2.8** or **2.4, 2.9** and **2.7**. The ultimate reductive elimination (**Eq. 2.10**) leads to mass loss from the composite ($2 X^-$, with X^- = any reasonable leaving group, e.g. OH^- , CH_3COO^-) and regenerates sp^2 centers in the graphitic layer (increased electronic conductivity).

The enhanced conductivity manifests itself by the ca. 5 fold current response of the ferrocenium / ferrocene couple for scan number 2 and larger as compared to scan 1. At the same time the ferrocene anodic / cathodic peak potential separation drops from 126 mV in scan 1 to 82 mV in scan 6. According to the growing ferrocene response, the reduction of the GO is almost completed after two cycles. The transformation is also confirmed by the concomitant mass loss (see following EQCM, 2.4.3.2). As a result of reduction, the brown color of the composite turned to black, showing the graphitization of GO. The remaining small asymmetry of the CV peaks of PVFc may originate from different solvation of the reduced and oxidized state of the composite film.¹¹⁷

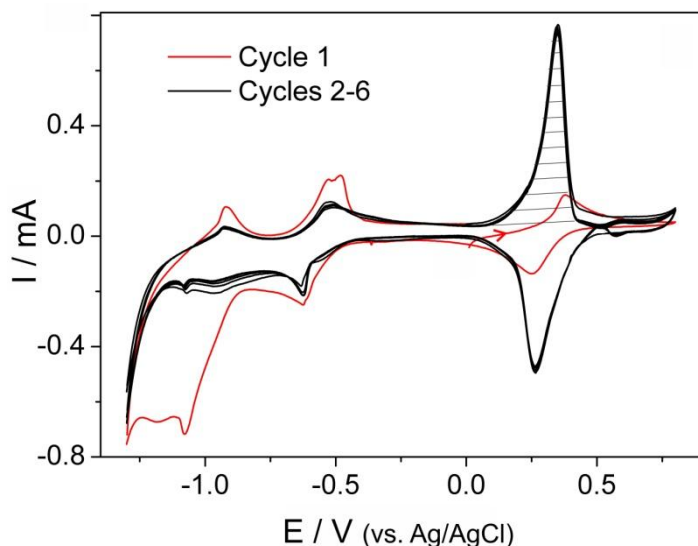


Figure 2.10. Repetitive CVs of $(\text{PVFc@GO})_{14}\text{@Au}$ corresponding to 2×10^7 mol subunits cm^{-2} in $0.1\text{M LiClO}_4/\text{H}_2\text{O} + 4\text{ mM MV}^{++}$ at $v = 20\text{ mV s}^{-1}$. First scan (red with arrow: $0 \rightarrow 0.8 \rightarrow 0\text{ V}$): small PVFc response, 1st scan continuation (red, $0 \rightarrow -1.3$) $\text{MV}^{++} \rightarrow \text{MV}^{\bullet+}$ and $\text{MV}^{\bullet+} \rightarrow \text{MV}^0$ reduction + electrocatalysis ($\text{GO} \rightarrow \text{rGO}$ transformation) + red. viologen deposition (sharp peaks); 2nd and later scans (black): see text for details (see sections 2.4.2.4 and 2.4.2.5 for experimental details).

In order to demonstrate the beneficial role of MV^{++} in the course of the electrochemical GO / rGO transition, the traditional electrochemical reduction was also checked. Guo et al. performed the electrochemical reduction using no electrocatalyst, but a more negative electrode potential (-1.5 V) and a more acidic solution ($\text{pH} = 5$).¹⁰⁷ The $(\text{PVFc@rGO})_2\text{@GC}$ prepared from $(\text{PVFc@GO})_2\text{@GC}$ with our new electrocatalytic procedure is much faster ready and shows in $0.1\text{M LiClO}_4/\text{MeCN}$ a 1.6 times higher coulombic efficiency than observed for the composite reduced without electrocatalyst (**Figure 2.11**).

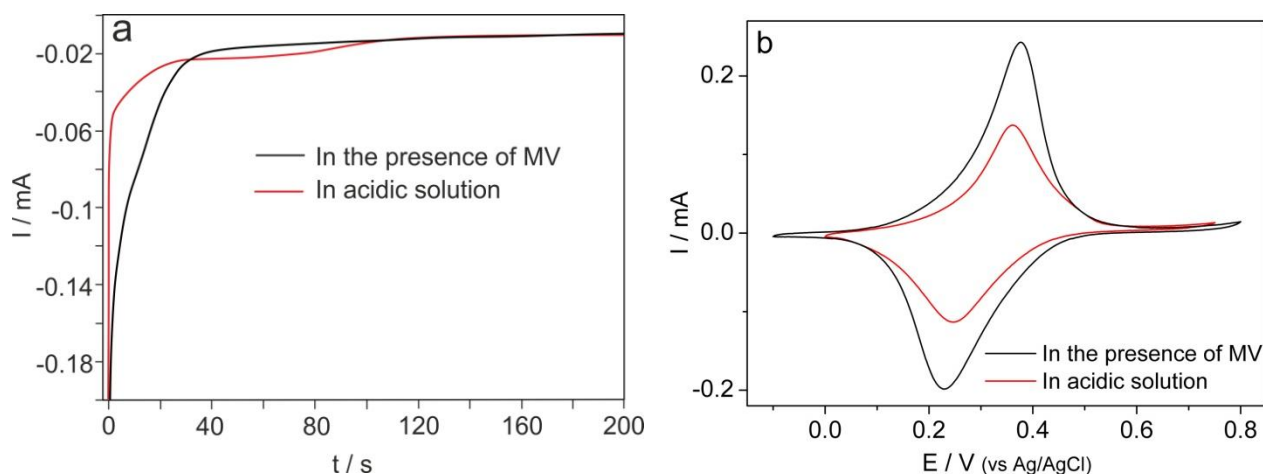


Figure 2.11. **a)** Controlled potential reduction and amperometric analyses of $(\text{PVFc@GO})_2\text{@GC}$ by applying a constant potential of -1.1 V (vs. Ag/AgCl) for 200 seconds in acidic solution (pH 5.0, $\text{K}_2\text{HPO}_4/\text{KH}_2\text{PO}_4$) (red) and in the presence of 4 mM MV^{++} (black). In both cases LiClO_4 was used as supporting electrolyte. The reduction process in the presence of MV was completed in ~ 40 seconds but in acidic solution >100 seconds were necessary. **b)** CV's of the corresponding $(\text{PVFc@rGO})_2\text{@GC}$ (after reduction in acidic solution (black) and after reduction in the presence of MV^{++} (red)) in 0.1M $\text{LiClO}_4/\text{MeCN}$ at $v=50$ mV s^{-1} . The electrode prepared by the electrocatalytic route shows a higher peak current and more charge under the CV trace as compared to the electrode prepared by the traditional, uncatalyzed reduction (see sections 2.4.2.4 and 2.4.2.5 for experimental details).

As discussed already above, the ratio of electroactive polymer to conductive filler influences the properties of the composite, such as electronic and ionic conductivity.⁶⁶ In order to find the best weight ratio ($\text{PVFc}^{x+} / \text{GO}^{\text{m-}}$) in the $(\text{PVFc@rGO})_6\text{@GC}$ composite material, a simple CV study was performed using electrodes (after GO / rGO transformation) with constant applied $\Gamma_{\text{PVFc}} = 3.4 \times 10^{-7}$ mol cm^{-2} (corresponding to 35 mC cm^{-2}) but varying $\text{PVFc}^{x+} / \text{GO}^{\text{m-}}$ weight ratio at different scan rates (**Figure 2.12**). The qualitative order of coulombic efficiencies (best to worst) for the different mixing ratios (different original GO content in %) is as follows: 4.4:1 (18.5 %) $>$ 2:1 (33 %) $>$ 6:1 (14 %) $>$ 8:1 (11%) $>$ 10:1 (9 %) $>$ 1:0 (0 %). The best coulombic efficiencies over the whole range of scan rates are achieved with a weight ratio of 4.4:1 corresponding to 18.5% original GO content. Obviously, kinetics are rather controlled by ionic than by electronic conductivity at high rGO content. The 18.5% of GO for top collection efficiency translates into only ca. 11 % rGO content after the $\text{GO} \rightarrow \text{rGO}$ transformation (see EQCM part). Notably, high performance with the smallest possible amount of filler

is one of the main goals in modern battery research.¹⁸ In all of the following subchapters the ratio PVFc / GO = 4.4 is used.

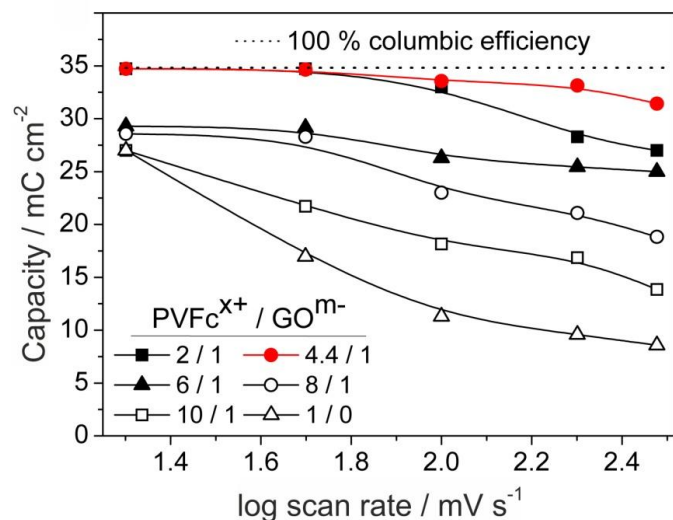


Figure 2.12. Anodic charge from (PVFc@rGO)₆@GC at constant PVFc surface concentration: 3.4×10^{-7} mol subunits cm⁻², from integration of the anodic PVFc wave (hatched region in Figure 2.10) after GO → rGO transformation as a function of log(scan rate), experimental values are spline function connected, other exp. conditions as in Figure 2.10 (See sections 2.4.2.3b, 2.4.2.4 and 2.4.2.5 for experimental details).

2.4.3.2. EQCM

The electrochemical quartz crystal microbalance (EQCM) was used in the past to demonstrate the gravimetric response of the compositional and mechanical changes on the electrode e.g., electrodeposition, supramolecular assembly and insertion / de-insertion of ions during charging-discharging under different dynamic condition.¹¹⁸⁻¹²² Here, EQCM was used to investigate the reductive elimination of oxygen-containing functional groups on GO during the GO / rGO transition. **Figure 2.13** shows the EQCM responses of (PVFc@GO)₁₄@Au for 6 repetitive cycles (corresponds to the CVs in Figure 2.10) in the potential ranges 0 → 0.8 → -1.3 → 0 V in the presence of MV. According to the CV (Figure 2.10), the scan starts with (PVFc@GO)₁₄@Au and after 2 to 3 scans the composite is transformed to (PVFc@rGO)₁₄@Au. In case of EQCM, a complicated frequency pattern is observed, but after 2-3 complete scans the response is a constant function. The relevant mass change is represented by the red dashed line, with $\Delta m = 3.9 \mu\text{g cm}^{-2}$. This value can be compared to the total mass of (PVFc@GO)₁₄@Au $51.5 \mu\text{g cm}^{-2}$ yielding the

percentage mass loss: $100 * \Delta m / (PVFc@GO)_{14}@Au = 7.6\%$ during the electrocatalytic reduction, which corresponds to 41 % weight loss of the GO weight content in the composite, remarkably close to 41-50% oxygen content claimed by “Graphenea”.

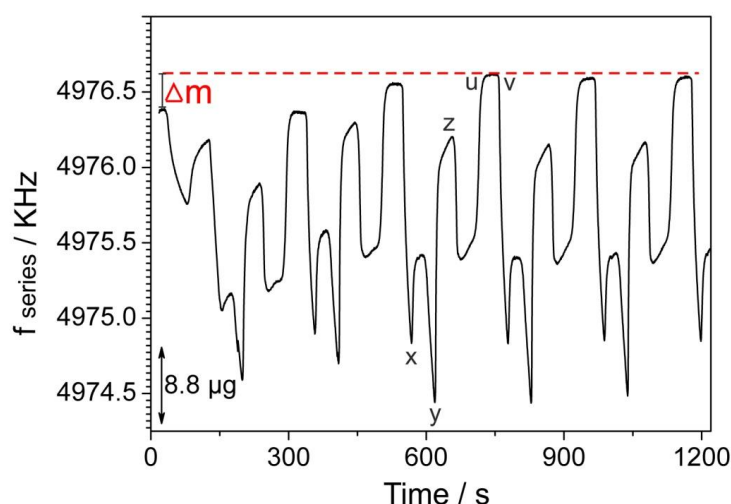


Figure 2.13. EQCM frequency responses for 6 consecutive CV-voltage scans $0 \rightarrow 0.8 \rightarrow -1.3 \rightarrow 0$ of $(PVFc@GO)_{14}@Au$ (mass density $51.5 \mu g cm^{-2}$) in $0.1M LiClO_4/H_2O + 4 mM MV^{++}$ at $v=20 mV s^{-1}$ (see Figure 2.10 for corresponding CV); mass density loss: $(\Delta m) = 3.9 \mu g cm^{-2}$ due to GO/rGO transformation from extrapolated irreversible change (dotted red line); x and y: reduction (Eq. 4 and 5) and deposition of reduced viologens; z: oxidation of reduced viologens; u, v: counter ion/solvent insertion/de-insertion upon Fc^+/Fc transition (see section 2.4.2.6 for experimental details)

The complicated reduction mechanism in the first 1.5 full scan in Figure 2.13 is studied by a combined CV (solid line) and EQCM frequency data (dashed line) involving the MV and PVFc redox waves (**Figure 2.14**). The frequency data obtained during the first anodic voltammetric scan over the PVFc redox couple (dashed I, blue trace) shows a mass increase during the oxidation of the ferrocene moieties, which can be interpreted as the insertion of ClO_4^- and water molecules into the composite film. The frequency did not return to its original value upon completion of the cycle, which points to irreversibly entrapped water molecules in the composite material. Previous EQCM studies have revealed that during oxidation of a film of PVFc with ClO_4^- as anion of the supporting electrolyte, one anion is inserted into the unhydrated film to compensate each positive charge with accompanying water molecules.¹²³⁻¹²⁴ Further scanning of the potential (dashed II, red trace) to the negative values (across the two MV waves) resulted in small increase in the weight of composite even though the reduction of GO causes weight loss.

This weight gain can be explained by diffusion / deposition of MV molecules inside the composite film. Oxidation of MV molecules causes their desorption from the composite film, and therefore an increase in the frequency is observed. However, the frequency does not reach its original value, due to the reduction of GO. As was expected, during the oxidation of PVFc in the second cycle, the composite weight was increased by the insertion of anions, whereas its reduction resulted in a weight change to a much lower value. This shows that the removal of MV is accelerated during the redox reactions of PVFc, possibly due to the electrostatic repulsion between MV^{++} and $PVFc^+$.

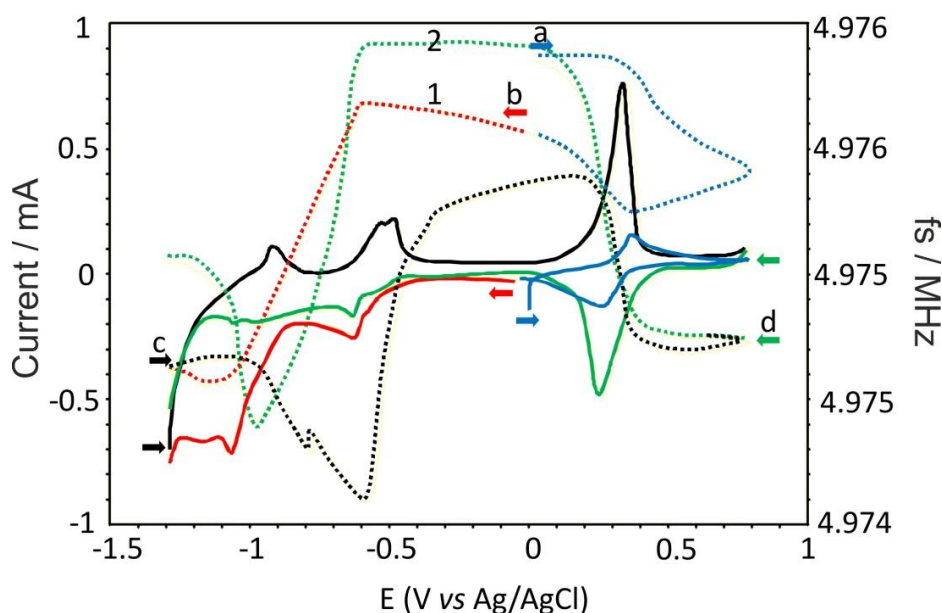


Figure 2.14. Combined CV (solid line) and EQCM frequency data (dashed line) of $(PVFc@GO)_{14}@Au$ for the first 1.5 full scans involving the redox waves of PVFc (ca. 0.3 V) and the waves of MV (-0.5 to -1 V) in aqueous 0.1M $LiClO_4/4\text{ mM } MV^{++}$ at $\nu=20\text{ mV s}^{-1}$ (compare Figure 2.10 and 2.13), blue (I) first scan over the Fc couple ($0 \rightarrow 0.8 \rightarrow 0\text{ V}$), followed by (red, II, $0 \rightarrow -1.3\text{ V}$) first cathodic scan over the MV^{++}/MV^+ and MV^+/MV couples, followed by black (III, $-1.3 \rightarrow +0.8\text{ V}$), followed by the second cathodic scan $0.8 \rightarrow -1.3\text{ V}$ (green, IV) (see section 2.4.2.6 for experimental details).

EQCM was also used to study the redox driven ion movement in the $PVFc@rGO$ material under potential cycling conditions. The $(PVFc@rGO)_{14}@Au$ electrode in the same 0.1M $LiClO_4/H_2O$ electrolyte but in absence of MV^{++} (after the GO / rGO

transition) shows a much more simple EQCM response (**Figure 2.15**). The spikes for viologen deposition and dissolution have disappeared. Mass change is now only related to the redox behavior of the ferrocenium / ferrocene couple and interpreted as ClO_4^- counter ion insertion (possibly accompanied water movement) into the composite upon oxidation and its reversible release upon reduction. The observed mass density change of $20.1 \mu\text{g cm}^{-2}$ corresponds to 39 % of the originally applied $(\text{PVFc@GO})_{14}$ or 42 % of the final $(\text{PVFc@rGO})_{14}\text{@Au}$. Thus, for the $42 \mu\text{g}$ pure PVFc content (subunit MW: 212.1 g/mol) a moving mass of $20.1 \mu\text{g}$ due to ClO_4^- (MW = 99.5) with an experimental mass ratio of $42 / 20.1 = 2.08$ is observed, as expected for the theoretical moving mass weight ratio $212.1 / 99.5 = 2.13$. Within experimental error these data indicate little or no accompanying water movement as already reported for pure PVFc modified electrodes.¹²⁴

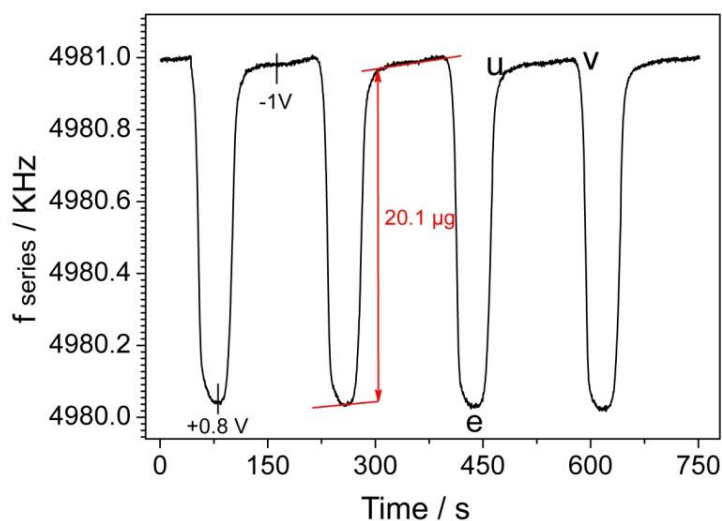


Figure 2.15. $(\text{PVFc@rGO})_{14}\text{@Au}$ in absence of viologen (other conditions as in a)); 4 consecutive voltage scans; e: Fc^+ plateau state barely reached, u,v= Fc plateau state extended (see section 2.4.2.6 for experimental details).

2.4.3.3. Electrochemical-AFM

Previous XRD analyses have shown that the layer to layer distance (d-spacing) of graphite oxide is 0.849 nm , which is larger than pristine graphite (0.335 nm). This is due to the presence of intercalated water molecules between layers as well as GO's functional groups. As it is expected, GO reduction again reduces the distance between layers, which is due to the removal of water molecules and functional groups. In the present study, an

electrochemical AFM method was used to investigate the height change after GO reduction. The composite height in the as prepared (PVFc@GO)@GC electrode under 0V potential was 560 nm (**Figure 2.16a-1**). After GO / rGO transition (GO reduction as in Figure 2.10), the height of composite decreased to 517 nm (at 0V), which shows 7.7% height decrease upon reduction (**Figure 2.16a-2**). It is interesting to compare mass changes from EQCM with the corresponding height changes obtained from electrochemical AFM. Thus, for the irreversible GO / rGO transition 7.6 % total mass reduction and 7.7% total height decrease was observed.

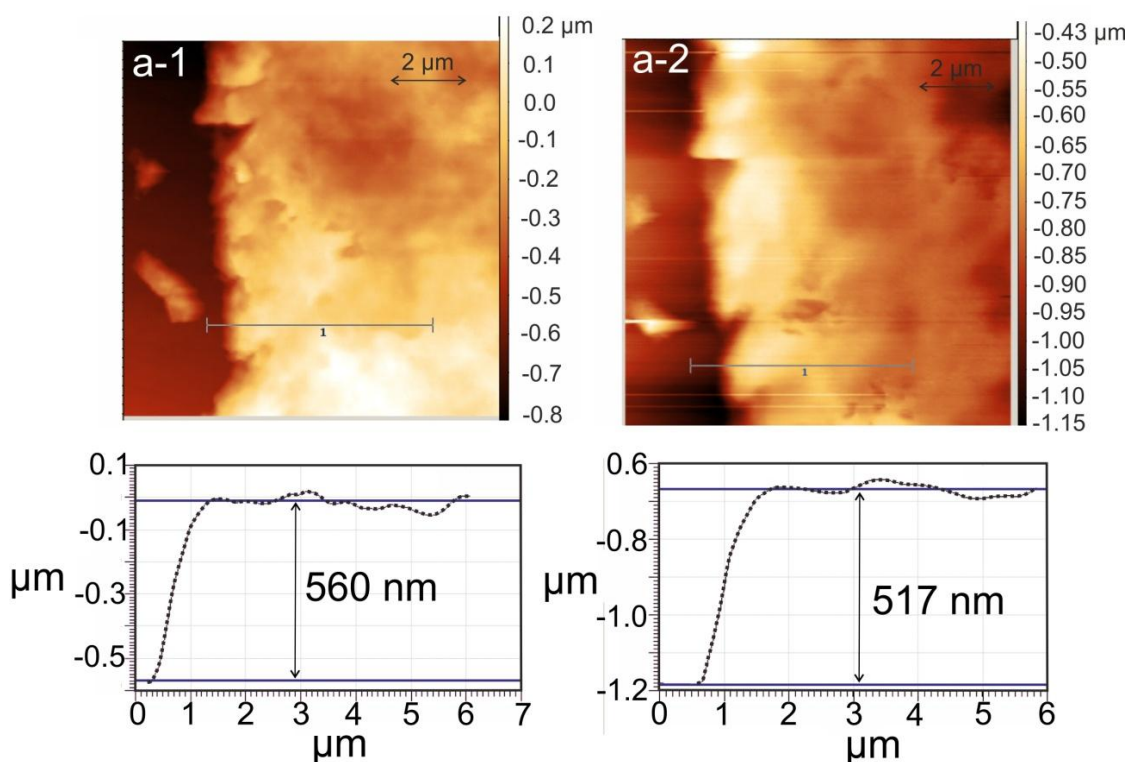


Figure 2.16. Electrochemical AFM analyses of the same region before (a-1) (PVFc@GO)@GC and after (a-2) (PVFc@rGO)@GC GO/rGO transition, both measured under potential = 0 V in aqueous 0.1M LiClO₄/4mM MV⁺⁺; arbitrarily selected cross sections at the same place indicate a decrease of height between the GC plane (left) and the composite top from 560 to 517 nm due to the GO/rGO transition (see sections 2.4.2.4 and 2.4.2.9 for electrode preparation and EC-AFM analysis, respectively).

The reduced composite was also analyzed by AFM in dry state to assess its morphology. The composite shows a relatively homogeneous structure all over the

electrode. Interestingly, mesoporous morphology throughout the composite film is observed (**Figure 2.17**).

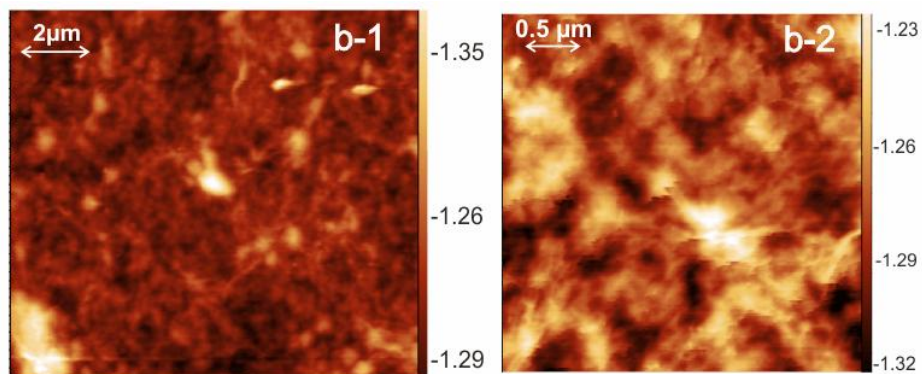


Figure 2.17. AFM images of (PVFc@rGO)@GC in the dry state with scan length of ca. 10.5 μm (**b-1**) and scan length of 3.3 μm (**b-2**) (see section 2.3.3.6 for experimental details).

The repeating ion insertion / de-insertion cycles during charging-discharging affect the porous structure of redox material as well as its dimension and mechanical stability. Particle pulverization, loss / weakening of electrical contact between redox material / conductive filler and redox material / current collector are some consequences of volume change of the electrode.¹²⁵ The charging-discharging of intercalation electrodes is based on the Li ion transport through the Li conductive planes within large individual particles (Cathode diameter > 1 μm and anode diameter > 5 μm). The rigid crystalline structures of intercalated cathodic materials provide low-volume expansion upon lithiation / delithiation (7%).¹²⁶ However, the amorphous structure of organic / organometallic polymers allows structural changes during ion insertion / de-insertion, which results in a phenomenon called ion breathing. Moreover, in contrary to Li-ion batteries, the percolation in the cathodic organic material is not limited to Li ions but allows other cations or in some cases even anion movement. Therefore, it is important to gain basic information on this phenomenon.

The ion breathing of PVFc@GO is accompanied by a reversible mass change (EQCM) during potential cycling. In the following experiment the oscillation of mass connected to an oscillation of the polymer height using electrochemical atomic force microscopy is shown (**Figure 2.18**). Instead of a linear potential scan as in the EQCM experiment, a square wave potential (0 \rightarrow +0.8 \rightarrow 0 \rightarrow ) with 30 s step time was applied

to the working electrode (PVFc@rGO)_nGC. Thus, during complete picture acquisition, which takes 400 s, 13 potential switches (30 s) of the redox state of the whole PVFc composite have occurred, and the 13 stripes in the final AFM image reflect the two states (dark: down, light: up). As seen from the amperometric current spikes, and from the sharp height transitions in the AFM image, the response is in the range of a second. The average height of the reduced PVFc composite above the scratched GC area (left) is 223 nm, and 256 nm for the oxidized PVFc⁺ composite yielding 33 nm average height breathing, i.e. 13 % of the (PVFc@rGO)_nGC height (**Table 2.1**). Local oxidative height increase of a polyferrocene was reported recently, but the electrochemical conditions were not well-defined¹²⁷ and multiple electrochemical switching of a ferrocene monolayer during an AFM scan with "stripes" based on local conductivity were observed.¹²⁸

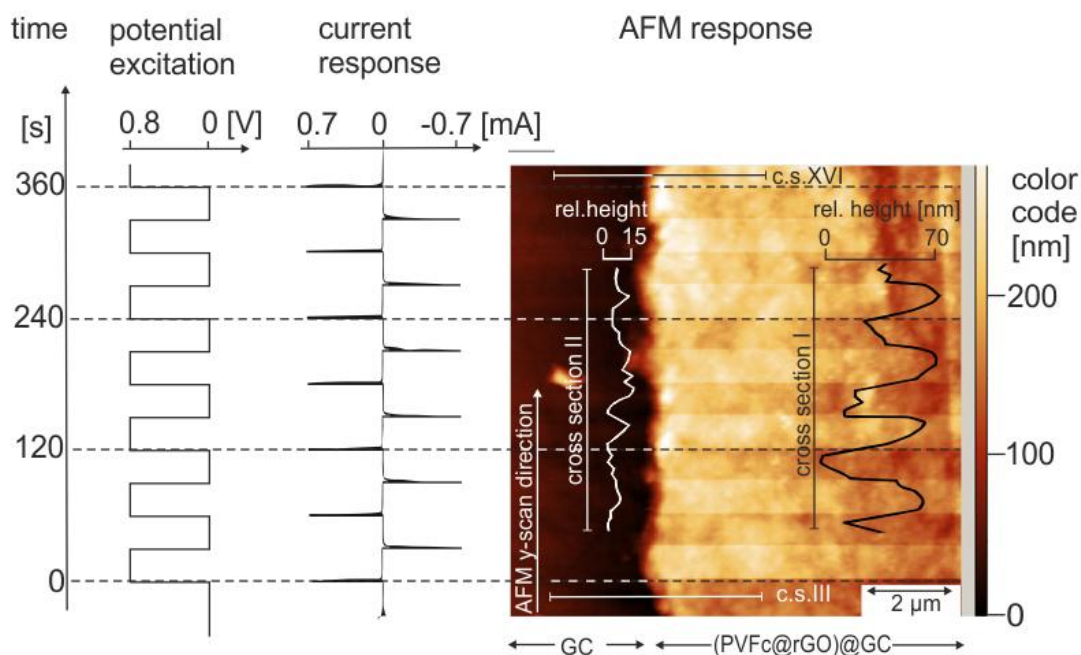


Figure 2.18. Electrochemical redox switching of (PVFc@rGO)_nGC during AFM image acquisition. Electrochemistry: electrolyte: 0.1 M LiClO₄/H₂O, excitation: square wave potential: 0→+0.8→0→ ... (13 steps with 30 s step time), current response (chronoamperometric): anodic (positive current (left)) and cathodic spikes. AFM image: (PVFc@rGO)_nGC (0.95 μg PVFc@rGO with weight ratio PVFc^{x+} / GO^{m-} = 4.4) on 0.07 cm² GC corresponding to $\Gamma_{\text{PVFc}} = 5.7 \times 10^{-8} \text{ mol cm}^{-2}$; left part of image: GC (PVFc@rGO scratched away), AFM scan direction upwards, total AFM acquisition time: 400s, 13 potential steps during AFM acquisition correlate with 13 stripes (dark/light) in the composite covered region but not in the scratched region (vertical cross section I and II in y-direction): typical height increase upon oxidation: 20 to 60 nm; averaged height change: 13 % (see Table 2.1 and sections 2.4.2.4 and 2.4.2.9 for electrode preparation and EC-AFM analysis, respectively)

As it was mentioned, the calculated difference between the averaged heights of oxidized and reduced states is 32.4 nm, i.e., 13 % with respect to GO and 15 % with respect to rGO ($\Gamma_{\text{Ferrocene subunits}} = 0.47 * 10^{-6} \text{ g} / (212 \text{ g mol}^{-1} * 0.07 \text{ cm}^2) = 3.1 * 10^{-8} \text{ mol subunits cm}^{-2}$) (Table 2.1).

	Oxidized:	Reduced
	257	225
	245	232
	253	227
	266	226
	262	229
	246	238
	261	186
Sum:	1790	1563
Average:	255.714286	223.285714

Table 2.1. Height analysis of the multiple redox switched composite including all stripes for horizontal cross sections III to XVI (Figure 2.18).

Assuming isotropic behavior the composite during mass change, the volume decrease is $-\alpha_v = 3\alpha_L$, α_v = contraction coefficient in volume and α_L = contraction coefficient in length, i.e. $\alpha_v = 3 * 13 \% = 39 \%$. However, no clear contraction of the composite in the x-y plane during the GO / rGO transition could be observed by AFM, because of relatively low resolution. Obviously, ClO_4^- insertion leads to higher density of the composite material with only minor expansion. For an isotropic thermal expansion one would expect $\alpha_v = 3\alpha_L$, α_v = expansion coefficient in volume and α_L = expansion coefficient in length. In the current case, large density changes in the case of ClO_4^- breathing is expected.

2.4.3.4. Raman spectroscopy

The Raman spectroscopic quality of the rGO obtained by chemical and the electrocatalytic method were compared. For this purpose a well characterized GO, i.e. oxo-functionalized graphene oxide (oxo-G)^{110, 129-130} reduced by established chemical reduction methods,¹¹²⁻¹¹⁴ and reduced electrocatalytically was used (**Figure 2.19a**). The G-band at 1585 cm⁻¹ is assigned to the first-order scattering of the E_{2g} phonon from sp² carbon (graphene lattice) and the D-band at 1340 cm⁻¹ is a breathing mode of point phonons of A_{1g} symmetry, which needs activation by a defect. Sharpening of both bands as well as the increase of the ratio of I_D/I_G (from 1 to 2.6) upon reduction are evidence for the high quality of reduction using MV⁺⁺ (according to the model introduced in the literature, distance of defects: 2.5 nm, defect density: 0.5%), which is comparable to the best results obtained with chemical reduction procedures¹¹²⁻¹¹⁴ (details: Experimental Section). The D' band at 1618 cm⁻¹ (in Oxo-G was covered under the G band) was observed after reduction.^{110, 129-130}

2.4.3.5. Thermogravimetric analysis

Thermogravimetric analysis (TGA) was performed to further evaluate the level of reduction of the GO (**Figure 2.19b**). The PVFc showed > 95% weight loss at 470°C, which was due to the decomposition of the polymer backbone.¹³¹⁻¹³² The GO sample showed a sigmoidal weight loss (ca. 38%) centered around 180°C probably due to loss of interlamellar water at lower temperature and loss of oxygen-containing functionalities at higher temperatures.¹³³ The weight loss of 38% compares well with the oxygen content claimed by the provider, but 470°C is not sufficient for complete removal of all functionalities. Interestingly, the PVFc@rGO composite did not show any weight loss up to 390°C, pointing to the removal of majority of GO functional groups upon its transformation to rGO.¹³³⁻¹³⁴ The electrochemical changes of a thermally reduced composite is not studied.

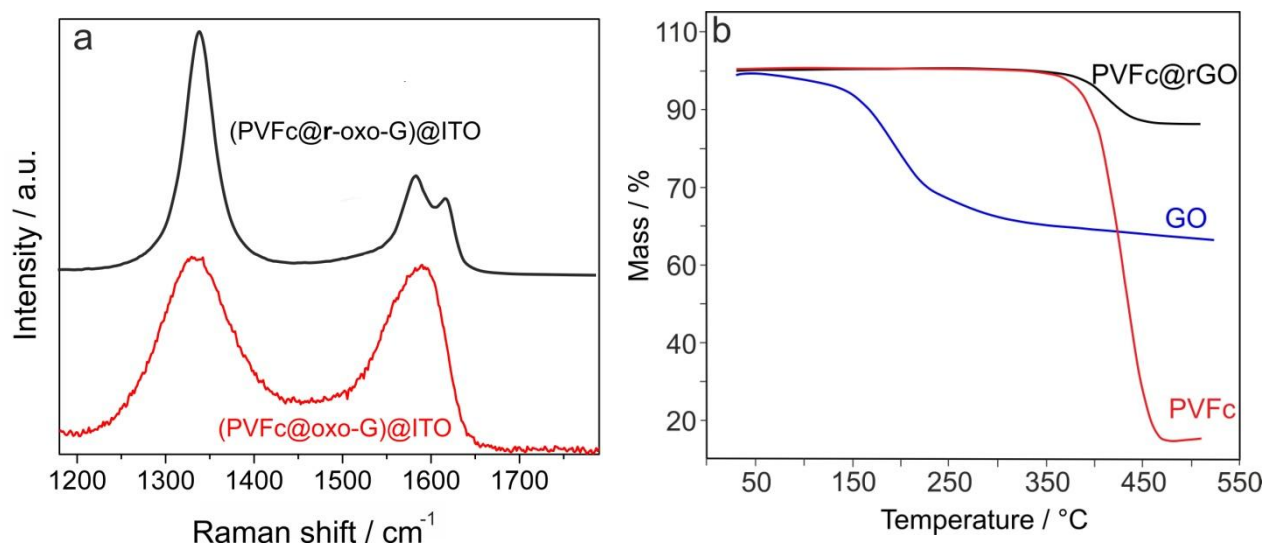


Figure 2.19. *a)* Raman spectra of (PVFc@oxo-G)@ITO (red) and (PVFc@r-oxo-G)@ITO (black) with weight ratio of PVFc/oxo-G=4.4; experimental conditions as in Figure 2.10. The full-width at half-maximum of the D and G bands of oxo-G are 134 cm^{-1} and 94 cm^{-1} and after reduction 39 cm^{-1} and 47 cm^{-1} , respectively. *b)* The thermogravimetric analyses (TGA) of GO (blue), PVFc (red), and PVFc@rGO composite (black) (prepared by an electrocatalytic reduction from a weight ratio of $\text{PVFc}^{x+} / \text{GO}^m = 4.4$) (see sections 2.4.2.1 and 2.4.2.8 for experimental details).

2.4.3.6. Electrical conductivity

The conductivity measured with an interdigitated microelectrode system showed a specific conductivity of $7.2 \times 10^{-4}\text{ S cm}^{-1}$ for the resulting PVFc@rGO (Exp. Sec. 2.4.2.7). The PVFc alone and GO alone were insulating. As far as the preparation of the composite was the same as for the electrodes preparation for battery tests, the same conductivity is expected. However, the electrolyte / solution may also influence the conductivity.

2.4.4. Summary

The electrochemical transformation of PVFc@GO to PVFc@rGO using methyl viologen dichloride (MV^{++}) as an electrocatalyst was studied in this subchapter (2.4). It was shown by different methods that MV^{++} can efficiently catalyze the reduction of GO. Compared to the traditional electrochemical method without electrocatalyst, the reduction process was faster and as it will be shown in the next subchapter, the reduction process in

thick layers (29 μm) was possible. The electrocatalytic role of MV^{++} , as well as efficient reduction of GO to rGO was shown by CV and EQCM. The irreversible GO / rGO transition resulted in 7.6% total mass reduction and 7.7% total height decrease. For the reversible ClO_4^- ion breathing, 42% mass increase upon oxidation was observed, which was accompanied by only 13% total height increase. The excellent quality of the MV catalyzed reduction was further shown by Raman spectroscopy and TGA.

2.5. Energy Storage Performances

2.5.1. Introduction

Ferrocene is a well-known reference electrode for electrochemical measurements. This is due to its remarkable electrochemical behavior in non-aqueous solution such as fast kinetics, reversibility, invariant redox potential toward other solutes, and air stability.¹³⁵ The redox potential (3.5 V vs. Li/Li⁺), as well as the high specific capacity (144 mAh g⁻¹) make ferrocene also a good candidate for high energy battery applications. Polymeric forms of ferrocene have been used for electron storage materials. Ferrocenes's subunit pendant on a main chain backbone shows not only reversible redox behavior, but also conductivity through electron hopping between redox sites.¹³⁶ However, the resulting conductivity is not enough for fast charging - discharging, nor for the preparation of the high areal-capacity electrodes. Therefore, many attempts shifted toward enhancing the conductivity through incorporation of conductive polymers into the poly-Ferrocene backbone or simply by addition of conductive fillers to the electrode matrix e.g., carbon fiber. Thus, Goodenough et al., have reported a ferrocene-containing polypyrrole cathodic material with 65 mAh g⁻¹ at 0.2 C and up to 2 μ m thickness.⁴⁵ Su; et al., reported on ferrocene-pyrrole-, ferrocene-triphenylamine-, and ferrocene-aniline polymers reaching 68 to 104 mAh g⁻¹, but these values do not include the weighted additional binder and conductive material used (50 wt%).^{54, 56-57} Notably, poly-pyrrole, -trialylamine or -aniline contribute capacitive properties into the material yielding an undesirable potential dependence in charging / discharging curves. In other cases, the conductivity of ferrocene-based polymer battery materials was achieved by loading carbon fillers in the polymer matrixes. The amount of active redox polymer in the final composition of the electrode was 40% for poly(ferrocenylsilane)⁴⁷ and only 10% for poly(ethynylferrocene), for poly(vinylferrocene) (PVFc) and polyferrocene.⁴⁶ The reported specific capacities (95 to 115 mAh g⁻¹) do not include the additional conductive agents and binders. If they are included the above values drop to 9.5 to 46 mAh g⁻¹, respectively, which considerably decreases the specific capacity of the electrodes. Therefore, in spite of the high capacity

of ferrocene (144 mAh g^{-1}), preparation of its polymeric form, as well as providing conductivity in the electrode materials significantly decreased the capacity so far.

2.5.2. Experimental

2.5.2.1. Instrument

The CVs and galvanostatic measurements were performed using an Autolab potentiostat (PGSTAT 20) interfaced to a computer with the GPS software (version 4.9).

2.5.2.2. Chemicals

The chemicals and solvents were purchased as it is mentioned in the section 2.4.2.2. Ethylene carbonate (anhydrous, 99%) and dimethyl carbonate (anhydrous, > 99%) are from Sigma-Aldrich.

2.5.2.3. Battery performance tests

The electrodes were prepared as it is explained in 2.4.2.4 and 2.4.2.5. Most battery performance tests were done in anhydrous 0.1M $\text{LiClO}_4/\text{MeCN}$, and a few in 0.1M $\text{LiClO}_4/\text{EC-DMC}$ using the polymer or composite ($\text{PVFc} / \text{GO} = 4.4$) modified GC working electrode.

2.5.3. Results and discussion

The electrochemical performance of the composite material was characterized by CV and by galvanostatic charge–discharge tests on $(\text{PVFc}@r\text{GO})_n@\text{GC}$ electrodes (chapter 2.4 and Experimental Section). In **Figure 2.20a** CVs of pure $(\text{PVFc}^{\text{x}+} \cdot \text{xNO}_3^-)_2@\text{GC}$ and $(\text{PVFc}@r\text{GO})_2@\text{GC}$ in 0.1 M $\text{LiClO}_4 / \text{H}_2\text{O}$ electrolyte are shown. As already discussed in chapter 2.4, the reversible wave at ca. 0.3 V is attributed to the fast, surface confined ferrocenium / ferrocene couple (Eq. 2.6). Kinetics and the amount of injectable

charge are obviously improved in $(\text{PVFc@rGO})_2\text{@GC}$ as compared to $(\text{PVFc}^{x+} \cdot x\text{NO}_3^-)_2\text{@GC}$. The redox wave of the polymer–graphene composite in acetonitrile is 70 mV more positive than in water and exhibits smaller peak separation (40 mV) than in aqueous solution (peak separation: 104 mV) reflecting the preferential stabilization of ferrocenium by water as compared to MeCN (**Figure 2.20b**), and less solvational changes during the redox process in MeCN as compared to H_2O .

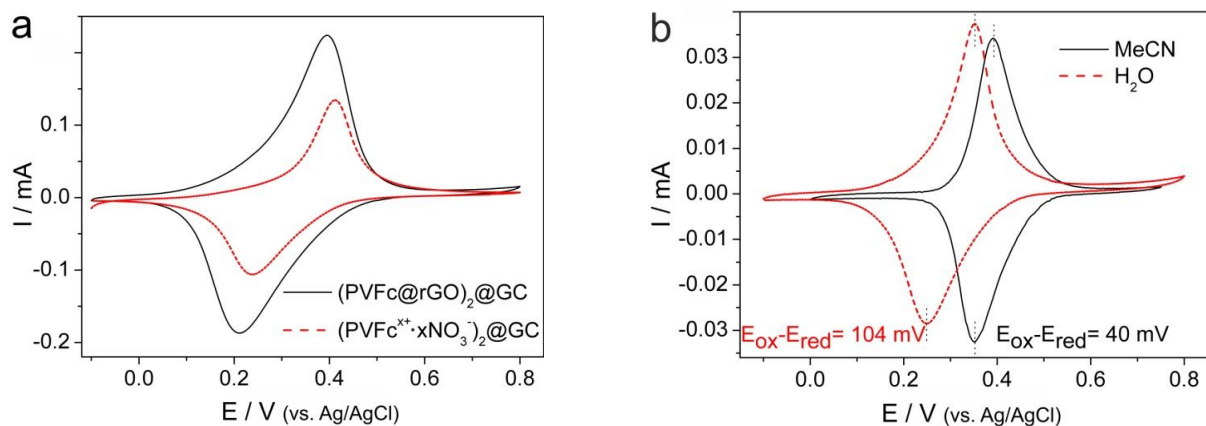


Figure 2.20. *a*) CVs of $(\text{PVFc@rGO})_2\text{@GC}$ (black, solid line) and $(\text{PVFc}^{x+} \cdot x\text{NO}_3^-)_2\text{@GC}$ (red, dashed line) in $0.1\text{M LiClO}_4/\text{H}_2\text{O}$, at $v = 50\text{mV s}^{-1}$. *b*) CVs of $(\text{PVFc@rGO})_1\text{@GC}$ in $0.1\text{M LiClO}_4/\text{H}_2\text{O}$ (dashed line, red) and in $0.1\text{M LiClO}_4/\text{MeCN}$ (solid line, black) at $v = 10\text{ mV s}^{-1}$.

A series of galvanostatic charge–discharge measurements on pure $(\text{PVFc}^{x+} \cdot x\text{NO}_3^-)_n\text{@GC}$ and on $(\text{PVFc@rGO})_x\text{@GC}$ (using the optimized 18.5% original GO content) were performed at different rates (1 A g^{-1} to 100 A g^{-1}) in $0.1\text{M LiClO}_4/\text{MeCN}$ using different layer thicknesses (number of drop casting steps, n) (**Figure 2.21**). A thin film ($n = 1$) of $(\text{PVFc}^{x+} \cdot x\text{NO}_3^-)_1\text{@GC}$ exhibits $\sim 98\%$ capacity at rates below 10 A g^{-1} and still more than 90 % at a rate of 100 A g^{-1} , i.e. comparable to the thin layer $(\text{PVFc@rGO})_2\text{@GC}$ (Figure 2.21a). The importance of the rGO as a performance enhancing additive becomes clear only for thicker layers with higher specific capacities. Figure 2.21 show clearly that for increasing layer thicknesses ($n = 1, 5.5, 9$ (a) and $n = 2$ (b)) at fast discharging (100 A g^{-1}), the observed capacity fades for $(\text{PVFc}^{x+} \cdot x\text{NO}_3^-)_n\text{@GC}$.

)_n@GC but not for (PVFc@rGO)_n@GC. Thus at 100 A g⁻¹ discharge rate and a layer thickness of n = 9, the capacity loss for (PVFc^{x+}·xNO₃⁻)_n@GC is 98% whereas for (PVFc@rGO)_n@GC it is only 30%.

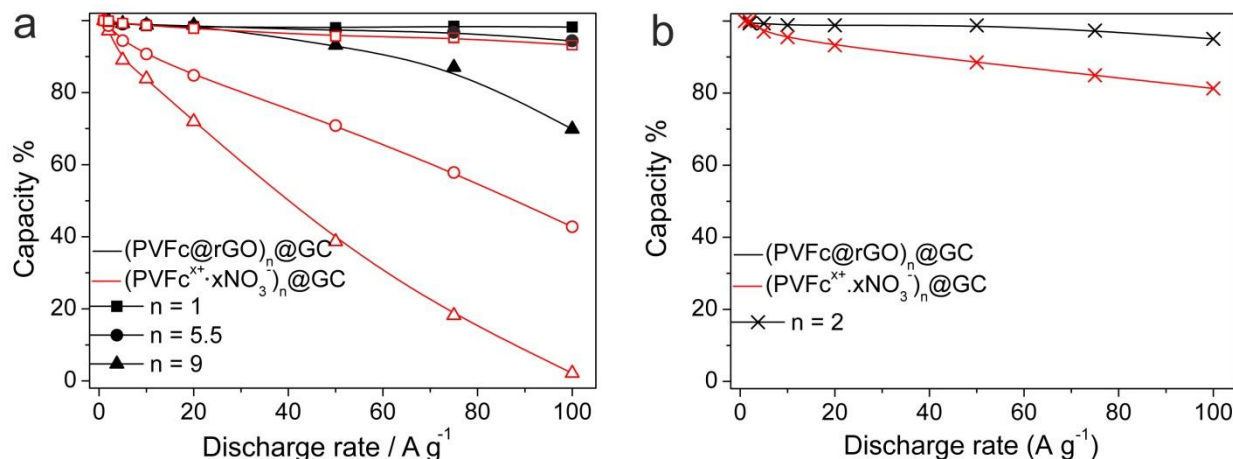


Figure 2.21. Percentage of observed capacity as a function of film thickness (n), n=1, 5.5, 9 (a) and n=2 (b) and as a function of discharge rates of (PVFc^{x+}·xNO₃⁻)_n@GC (symbols, red) and (PVFc@rGO)_n@GC (filled symbols, black) from galvanostatic measurements (values were fitted with a spline function).

A preliminary test in the well-known battery solvent - ethylene carbonate / dimethyl carbonate (EC:DMC) (1:1 vol %) using 0.1M LiClO₄ - was performed. In **Figure 2.22a** CV of (PVFc@rGO)₂@GC in EC:DMC electrolyte is shown. Kinetics are clearly slower as compared to the same composite in MeCN electrolyte (Figure 2.20). The redox wave of the polymer-graphene composite in MeCN exhibits smaller peak separation (40 mV) than in EC:DMC (1:1) solution (233 mV) reflecting less polarization in MeCN. The capacity decay for a film of (PVFc@rGO)₂@GC at current rate of 100 A g⁻¹ in EC:DMC was 30 % (**Figure 2.22b**) compared to MeCN, which was only 2% (Figure 2.21a). However, the capacity decay at the slowest charging rate in both solutions were < 1%.

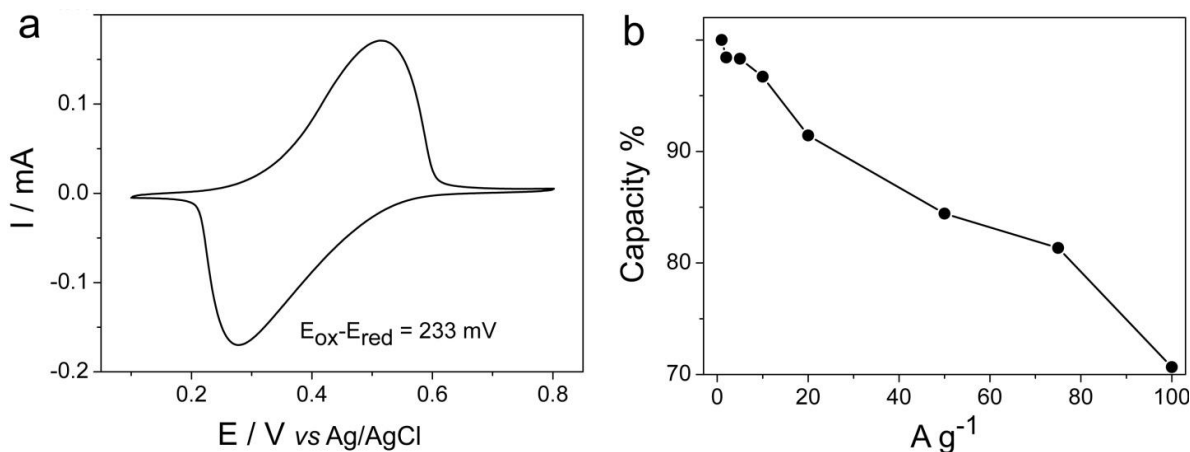


Figure 2.22. *a)* CV of $(\text{PVFc@rGO})_2\text{@GC}$ at $v=50 \text{ mV s}^{-1}$ in $\text{EC:DMC (1:1)} / 0.1\text{M LiClO}_4$; *b)* Percentage of observed capacity as a function of discharge rate of $(\text{PVFc@rGO})\text{@GC}$, obtained by the galvanostatic charge–discharge tests. Electrochemical condition as in a).

As shown in **Figure 2.23**, the observed capacity of $(\text{PVFc@rGO})_n\text{@GC}$ increases linearly with layer thickness (equivalent to drop casting numbers n and $\Gamma_{\text{Fc subunits}}$) up to a specific capacity of 770 mC cm^{-2} (for $n = 137$). On the other hand, the capacity of the polymer alone, i.e. $(\text{PVFc}^{x+} \cdot x\text{NO}_3^-)_n\text{@GC}$, increases linearly only up to 65 mC cm^{-2} (corresponding to ca. $n = 17$ and a thickness of $3 \text{ }\mu\text{m}$) and for thicker films the specific capacity drops again (inset, Figure 2.23). It seems that ion and / or electron percolation is shutting down at a distance of ca. 400 nm in pure PVFc. In striking contrast, the rGO doped PVFc does not lose its activity over the 20-fold range of thickness.

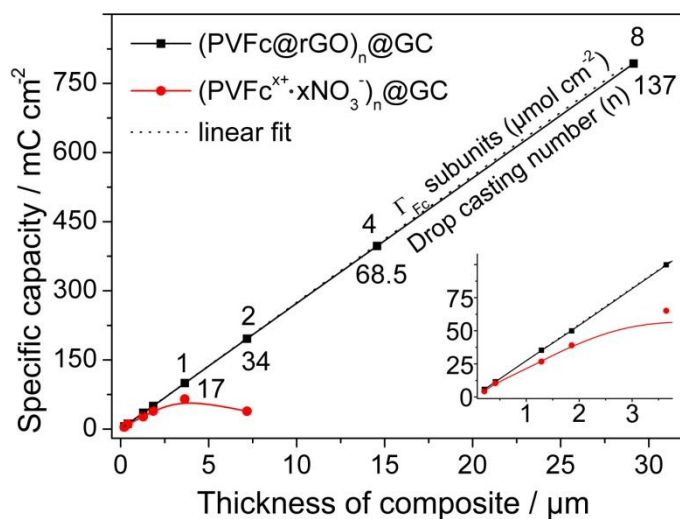


Figure 2.23. Accessible surface charge as a function of thicknesses of $(\text{PVFc@rGO})_n\text{@GC}$ ($-\blacksquare-$, black), and of $(\text{PVFc}^{x+} \cdot x\text{NO}_3^-)_n$ ($-\bullet-$, red); average film thickness for $n = 1$ is 210 nm .

The galvanostatic charge–discharge curves of $(\text{PVFc@rGO})_2\text{@GC}$ in 0.1M $\text{LiClO}_4/\text{MeCN}$ is shown in **Figure 2.24**. The charging–discharging curves are linear with a typical Nernstian 120 mV per 2 decades $[\text{FeIII}] / [\text{FeII}]$ behavior. The obtained discharge capacity of a composite composed of 81.5 wt% PVFc and 18.5 wt% original GO was 105.6 mAh g^{-1} . This points to $\sim 3 \text{ mAh g}^{-1}$ additional capacitive charge attributed to 12 wt% incorporated rGO sheets (based on EQCM, Figure 2.13). Thus $(\text{PVFc@rGO})_n\text{@GC}$ has a final capacity of 114 mAh g^{-1} with 88 wt% contribution from the electroactive polymer, i.e. it has a much higher electrochemically accessible ferrocene content than any previously reported polyferrocene–based cathodic materials.

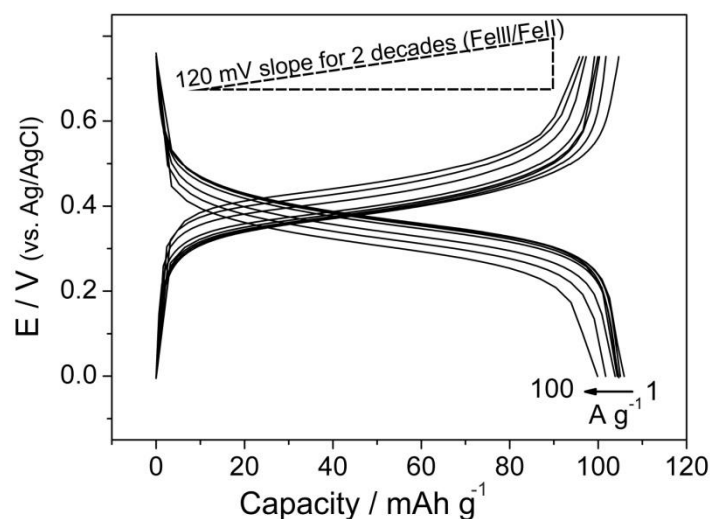


Figure 2.24. a) Galvanostatic charging–discharging curves of $(\text{PVFc@rGO})_2\text{@GC}$ at charging rates 1, 2, 5, 10, 20, 50, 75 and 100 A g^{-1} in 0.1M $\text{LiClO}_4/\text{MeCN}$.

The here reported performance values for $(\text{PVFc@rGO})_n\text{@GC}$ are also remarkable with respect to the well–known radical based nitroxide–containing polymers.^{71–72} Thus, for example K. Koshika et al. reported an “ultrafast chargeable polymer electrode”, in which a 3 mC cm^{-2} film of poly(2,2,6,6–tetramethylpiperidinyloxy–4–yl vinyl ether) is charged to 97% in 3 seconds in aqueous electrolyte,⁷¹ while in the present study a film of $(\text{PVFc@rGO})_1\text{@GC}$ with a capacity of 5.8 mC cm^{-2} ($n = 1$) is discharged $> 98\%$ in 2.8 seconds. The thicker films with capacities of even 11.57 ($n = 2$) and 32.8 ($n = 5.5$) mC cm^{-2} are 95% and 94% discharged in 3.1 and 3.8 seconds, respectively (Figure 2.21).

Moreover, due to the excellent electrical and ionic conductivity of the (PVFc@rGO)_n@GC composite, it is possible to apply much more electroactive material with areal charge density up to 770 mC cm⁻² (for n = 137, Figure 2.23) than previously reported in case of nitroxide radical polymers with a maximum reported areal charge density of only 150 mC cm⁻².⁷¹⁻⁷⁴

The cycling performance of (PVFc@rGO)₂@GC was ca. 95 % as observed in a charging–discharging galvanostatic test over 300 cycles using cutoff voltages of 0 and 0.75 V (vs. Ag/AgCl) at a fast charging–discharging rate of 10 A g⁻¹ (**Figure 2.25**).

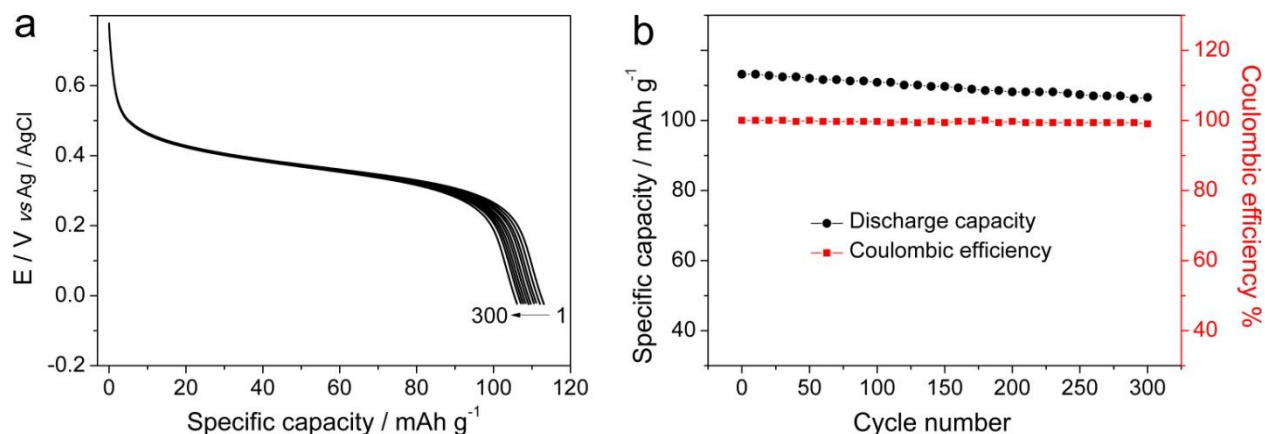


Figure 2.25. *a) Discharge curves of (PVFc@rGO)₂GC during 300 galvanostatic charge–discharge cycles in the cutoff voltages of 0 to 0.75 V (vs. Ag/AgCl) at 10 A g⁻¹ charging–discharging rate. b) Corresponding discharge capacity and coulombic efficiency of a). Every 30 cycles is displayed.*

2.5.4. Summary

In subchapter 2.5, the electrochemical behavior of polymer-rGO composite was studied. It was shown, that the injectable charge, as well as the kinetics in a thin film of pure polymer were much smaller than in the composite film. This binder-free composite film had a specific capacity 114 mAh g⁻¹ and it contained only 12% rGO as conductive filler. The obtained specific capacity was much higher than any previously reported

polyferrocene-based cathodic materials.^{45-47,54,56-57} Besides, the composite was demonstrated to be "thickness scalable" up to 770 mC cm⁻² corresponding to 29 μm with > 99% coulombic efficiency. However the scalability of the polymer alone was limited to 65 mC cm⁻². The charging rate of the composite was also remarkable, e. g., a film of (PVFc@rGO)@GC with an observed capacity of 5.8 mC cm⁻² was > 98% charged in 2.8 seconds. This rate performance is higher than those reported for well-known high rate radical based nitroxide polymers.⁷¹⁻⁷² The improved electrochemical response of the composite such as thickness scalability and rate performance compared to the polymer alone, clearly indicated the role of rGO in providing an excellent ion / electron percolation system throughout the composite film. In addition, the composite material exhibited a perfect cycling stability by sustaining > 95% of the specific capacity over 300 charging–discharging galvanostatic cycles compared to its initial value.

Chapter 3

Summary and Outlook

3.1. Summary

In this thesis, the electrochemical energy storage capability of a nanocomposite consisting of poly(vinylferrocene) and reduced graphene oxide was studied. The appropriate redox potential (+0.3 V vs. Ag/AgCl), fast electrochemical kinetics and a stable voltage plateau make PVFc an excellent candidate for cathodic material. However, a big challenge facing organic-based materials for electrochemical energy storage is introducing ionic and electronic conductivity into the film composition. Because of the high surface area of organic polymers, addition of large amounts of conductive fillers (> 60 wt %) have been necessary so far. In this thesis, a new method was developed, which allows the preparation of nanocomposite materials with very small wt % of conductive filler. The resulting nanocomposite exhibited an excellent electrochemical response, with respect to the current density rate and the thickness scalability. Notably, this method is not only limited to the mentioned polymer, but can be expanded to a wide variety of cationic redox polymers. The method of preparation was carried out as follows:

I. Synthesis of the positively charged redox polymer. As far as the as-synthesized PVFc possesses no charge, a pre-oxidizing step was necessary ($\text{PVFc}^0 \rightarrow \text{PVFc}^+$). However, as shown in the subchapter 2.3, even partially oxidized PVFc ($\text{PVFc}^+ \rightarrow \text{PVFc}^{x+}$) was sufficient for the self assembly step (discussed in III).

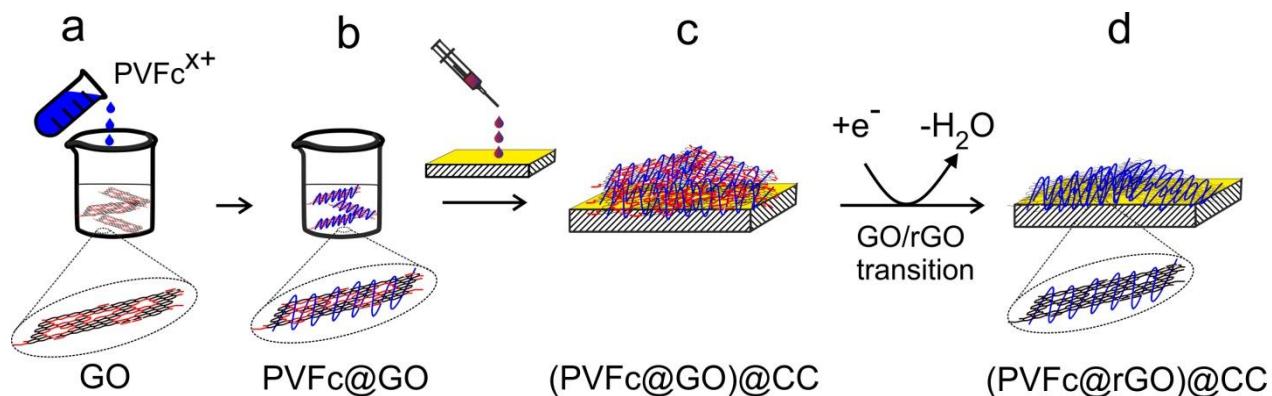
II. Preparation of well dispersed single GO sheets as a stable colloidal solution. This was obtained by appropriate dilution and sonification of a commercial graphene oxide solution.

III. The self-assembly was achieved based on the attractive electrostatic interaction between the partially oxidized polymer (PVFc^{x+}) and the negatively charged GO in the aqueous solution. This was attained by simply mixing the solutions of the two

components, followed by a short sonification step. Zeta potential measurements showed, that at a PVFc / GO ratio of 4.4, the polymer strands wended in close contact around the GO sheets. The experimental result was supported by a modeling study, which confirmed up to six polymer layers covering GO sheets. Thus the procedure developed here allowed the production of a colloidal solution, in which redox active polymers were in close contact with the so far non-conducting GO (Scheme 3.1 a→b).

IV. The deposition / drying of the colloidal solution on different current collectors was done by a simple drop-casting method and resulted in a modified electrode, in which the redox sites were still in contact to single GO sheets (confirmed by AFM images) (Scheme 3.1 b→c).

V: Transformation of PVFc@GO to PVFc@rGO using methyl viologen dichloride (MV^{++}) as an electrocatalyst. The electrocatalytic role of MV^{++} , as well as the efficient reduction of GO was shown by CV and EQCM. The electrocatalytic reduction provided high quality rGO, even in very thick layers (29 μm). The reduction process was very fast, an aqueous solution was used and the whole process was done at room temperature. The reduction step transformed the non-conducting GO into conductive rGO without destroying the supramolecular assembly (Scheme 3.1 c→d).



Scheme 3.1. Schematic representation of the preparation of (PVFc@rGO)@CC electrode.

It is demonstrated for the first time, that molecularly tightly connected graphene sheets - polymer strands can be produced efficiently by prior self-assembling of graphene oxide and partially oxidized, positively charged PVFc followed by an electrocatalytic reduction of GO to rGO. The use of supramolecular chemistry has opened a new avenue for the preparation of electron- and ion-percolation systems. It was found, that PVFc alone supports already the formation of mesoporous tunnels also by a kind of self-assembling even without the help of graphene oxide. Thus the preparation of ion percolation paths is naturally build-in. The partially stacked PVFc-separated graphene oxide observable by AFM at a weight ratio PVFc / GO = 1:1 showed the active percolation system for ions and electrons consisting of deep holes and closely spaced GO, i.e. rGO after reduction. The direct contact between rGO flakes might be necessary, but a ferrocenium / ferrocene electron shuttling mechanism between GO flakes could not be excluded. Anyhow, as shown in Figure 2.23, the conductivity of pure PVFc without rGO broke down after a few hundred nm film thickness.

The electrochemical performance of the nanocomposite was remarkable. The binder-free composite film containing only 12% rGO as conductive filler was demonstrated to be "thickness scalable" up to 0.21 mAh cm^{-2} corresponding to $29 \text{ }\mu\text{m}$ with $> 99\%$ coulombic efficiency. The PVFc@rGO film with an observed capacity of 5.8 mC cm^{-2} was $> 98\%$ charged in 2.8 s. This "rate performance" was considerably higher than those reported for the well-known high rate radical based nitroxide polymers.⁷¹⁻⁷² This outstanding energy storage capability was explained by the fast faradaic reaction in the organic solvent (i), the high rate electron transfer obtained by well dispersed rGO sheets in the composite matrix (ii) and the benefits to anion conduction, because of the increased surface area in the polymer-rGO nanocomposite (iii). The high areal-capacity combined with fast charging-discharging and a high cyclability places this energy storing material into the top range of the known organic battery materials. Notably, this composite material showed excellent performance in both organic and aqueous solutions.

It was impressive how well the experimental mass changes of the composite from EQCM fitted the theoretically expected mass changes for the GO / rGO transition. The

same was true for the ClO_4^- ion breathing, i.e. one anion accompanied by little or no water molecules was clearly identified. Briefing was also followed by a new method i.e. observation of the molecular height change during electrochemically triggered ion breathing. Thus, 13% height change was observed for PVFc@rGO. However, no systematic lateral contraction and expansion could be identified. The combination of electrochemical height breathing from EC-AFM and electrochemical mass breathing from EQCM must be considered a new technique and offers a more detailed insight into ion breathing than so far found in literature.

The ongoing research in our lab has shown that the principal procedure of self-assembling electroactive polymers on GO via stable colloidal solutions, leading to a mesoporous composite structure with excellent ion percolating properties is also applicable to other redox polymer / GO combinations.

3.2. Outlook

It would be interesting to extend the method of composite preparation also to other electroactive, positively charged redox polymers with electrochemical charge storing properties. Some polymers based on viologen, ferrocene and cobaltocenium have already undergone preliminary tests and showed promising responses.

Another interesting extension of the work would be to check alternative carbon materials with a negative surface charge, e.g., oxidized multi-walled carbon nanotube as conductive filler. The material is conductive and has a negative surface charge. Effectively, preliminary tests show redox polymer wrapping.

Alternative composite deposition techniques should be checked, e.g., electrodeposition, spraying, printing, spin coating etc). Such techniques may improve the material's performance and would be closer to the techniques applicable for mass production.

References

1. J. B. Goodenough, K.-S. Park, *J. Am. Chem. Soc.* **135**, 1167 (2013).
2. W. Li, J. R. Dahn, D. S. Wainwright, *Science* **264**, 1115 (1994).
3. B. J. Landi, M. J. Ganter, C. D. Cress *et al.*, *Energy Environ. Sci.* **2**, 638 (2009).
4. S. Afyon, F. Krumeich, C. Mensing *et al.*, *Sci. Rep.* **4**, 7113 (2014).
5. Z. Song, H. Zhou, *Energy Environ. Sci.* **6**, 2280 (2013).
6. S. M. Beladi-Mousavi, S. Sadaf, L. Walder *et al.*, *Adv. Energy Mater.* **6**, 1600108 (2016).
7. M. M. Thackeray, S.-H. Kang, C. S. Johnson *et al.*, *J. Mater. Chem.* **17**, 3112 (2007).
8. Y. Liang, Z. Tao, J. Chen, *Adv. Energy Mater.* **2**, 742 (2012).
9. W. Choi, D. Harada, K. Oyaizu, H. Nishide, *J. Am. Chem. Soc.* **133**, 19839 (2011).
10. N. Sano, W. Tomita, S. Hara *et al.*, *ACS Appl. Mater. Interfaces* **5**, 1355 (2013).
11. S. Sen, J. Saraidaridis, S. Y. Kim, G. T. R. Palmore, *ACS Appl. Mater. Interfaces* **5**, 7825 (2013).
12. T. Suga, H. Ohshiro, S. Sugita *et al.*, *Adv. Mater.* **21**, 1627 (2009).
13. M. E. Spahr, in *Lithium-Ion Batteries: Science and Technologies*, M. Yoshio, R. J. Brodd, A. Kozawa, Eds. (Springer New York, New York, NY, 2009), pp. 117-154.
14. A. Manthiram, Y. Fu, S.-H. Chung, C. Zu, Y.-S. Su, *Chem. Rev.* **114**, 11751 (2014).
15. H.-g. Wang, S. Yuan, D.-l. Ma *et al.*, *Adv. Energy Mater.* **4**, 1301651 (2014).
16. X. Han, C. Chang, L. Yuan, T. Sun, J. Sun, *Adv. Mater.* **19**, 1616 (2007).
17. K. Oyaizu, Y. Ando, H. Konishi, H. Nishide, *J. Am. Chem. Soc.* **130**, 14459 (2008).
18. Z. Song, T. Xu, M. L. Gordin *et al.*, *Nano Lett.* **12**, 2205 (2012).
19. A. Usuki, N. Hasegawa, M. Kato, S. Kobayashi, in *Inorganic Polymeric Nanocomposites and Membranes*. (Springer Berlin Heidelberg, 2005), vol. 179, pp. 135-195.
20. T. Ramanathan, S. Stankovich *et al.*, *J. Polym. Sci. Part B: Polym. Phys.* **45**, 2097 (2007).
21. T. Ramanathan, A. A. Abdala, S. Stankovich *et al.*, *Nat. Nanotechnol.* **3**, 327 (2008).
22. E. Hwang, S. Seo, S. Bak *et al.*, *Adv. Mater.* **26**, 5129 (2014).
23. L. Al-Mashat, K. Shin, K. Kalantar-zadeh *et al.*, *J. Phys. Chem. C* **114**, 16168 (2010).
24. P. You, Z. Liu, Q. Tai *Adv. Mater.* **27**, 3632 (2015).
25. Z. Zhu, J. Ma, Z. Wang *et al.*, *J. Am. Chem. Soc.* **136**, 3760 (2014).
26. W. Guo, Y.-X. Yin, S. Xin *et al.*, *Energy Environ. Sci.* **5**, 5221 (2012).
27. R. Verdejo, M. M. Bernal, L. J. Romasanta, M. A. Lopez-Manchado, *J. Mater. Chem.* **21**, 3301 (2011).
28. Y. Zhu, S. Murali, W. Cai *et al.*, *Adv. Mater.* **22**, 3906 (2010).
29. L. Feng, S. Zhang, Z. Liu, *Nanoscale* **3**, 1252 (2011).
30. T. Kim, H. Lee, J. Kim, K. S. Suh, *ACS Nano* **4**, 1612 (2010).
31. M. Zhang, B.-C. Yin, X.-F. Wang, B.-C. Ye, *Chem. Commun.* **47**, 2399 (2011).
32. S. Li, A. N. Aphale, I. G. MacwanS *et al.*, *ACS Appl. Mater. Interfaces* **4**, 7069 (2012).
33. D. R. Dreyer, S. Park, C. W. Bielawski, R. S. Ruoff, *Chem. Soc. Rev.* **39**, 228 (2010).
34. S. Park, J. An, J. R. Potts *et al.*, *Carbon* **49**, 3019 (2011).
35. N.-J. Song, C.-M. Chen, C. Lu *et al.*, *J. Mater. Chem. A* **2**, 16563 (2014).
36. M. Armand, J. M. Tarascon, *Nature* **451**, 652 (2008).
37. F. Cheng, J. Liang, Z. Tao, J. Chen, *Adv. Mater.* **23**, 1695 (2011).
38. V. Etacheri, R. Marom, R. Elazari *et al.*, *Energy Environ. Sci.* **4**, 3243 (2011).
39. J. B. Goodenough, Y. Kim, *Chem. Mater.* **22**, 587 (2010).
40. P. Poizot, F. Dolhem, *Energy Environ. Sci.* **4**, 2003 (2011).
41. X. Mao, F. Simeon, D. S. Achilleos *et al.*, *J. Mater. Chem. A* **1**, 13120 (2013).
42. X. Mao, G. C. Rutledge, T. A. Hatton, *Langmuir* **29**, 9626 (2013).
43. L. Cao, S. Sadaf, S. M. Beladi-Mousavi, L. Walder, *Eur. Polym. J.* **49**, 1923 (2013).
44. R. R. Gagne, C. A. Koval, G. C. Lisensky, *Inorg. Chem.* **19**, 2854 (1980).
45. K. S. Park, S. B. Schougaard, J. B. Goodenough, *Adv. Mater.* **19**, 848 (2007).

46. K. Tamura, N. Akutagawa, M. Satoh *et al.*, *Macromol. Rapid Commun.* **29**, 1944 (2008).
47. H. Zhong, G. Wang, Z. Song *et al.*, *Chem. Commun.* **50**, 6768 (2014).
48. Y. Ding, Y. Zhao, G. Yu, *Nano Lett.* **15**, 4108 (2015).
49. T. Kawai, C. Iwakura, H. Yoneyama, *Electrochim. Acta* **34**, 1357 (1989).
50. R. H. Staff, M. Gallei, M. Mazurowski *et al.*, *ACS Nano* **6**, 9042 (2012).
51. J. Elbert, J. Mersini, N. Vilbrandt *et al.*, *Macromolecules* **46**, 4255 (2013).
52. J. Elbert, M. Gallei, C. Rüttiger *et al.*, *Organometallics* **32**, 5873 (2013).
53. J. Elbert, F. Krohm, C. Rüttiger *et al.*, *Adv. Funct. Mater.* **24**, 1591 (2014).
54. C. Su, L. Ji, L. Xu *et al.*, *RSC Adv.* **5**, 14053 (2015).
55. J. Xiang, R. Burges, B. Häupler *et al.*, *Polymer* **68**, 328 (2015).
56. C. Su, L. Wang, L. Xu, C. Zhang, *Electrochim. Acta* **104**, 302 (2013).
57. C. Su, Y. Ye, L. Xu, C. Zhang, *J. Mater. Chem.* **22**, 22658 (2012).
58. W. Zheng, S.-C. Wong, *Compos. Sci. Tech.* **63**, 225 (2003).
59. E. T. Thostenson, Z. Ren, T.-W. Chou, *Compos. Sci. Tech.* **61**, 1899 (2001).
60. T. Ramanathan, H. Liu, L. C. Brinson, *J. Polym. Sci. Part B: Polym. Phys.* **43**, 2269 (2005).
61. T. Desai, P. Koblinski, S. K. Kumar, *J. Chem. Phys.* **122**, 134910 (2005).
62. F. W. Starr, T. B. Schröder, S. C. Glotzer, *Macromolecules* **35**, 4481 (2002).
63. H. He, J. Klinowski, M. Forster, A. Lerf, *Chem. Phys. Lett.* **287**, 53 (1998).
64. A. Lerf, H. He, M. Forster, J. Klinowski, *J. Phys. Chem. B* **102**, 4477 (1998).
65. S. Stankovich, R. D. Piner, X. Chen *et al.*, *J. Mater. Chem.* **16**, 155 (2006).
66. S. Stankovich, D. A. Dikin, G. H. B. Dommett *et al.*, *Nature* **442**, 282 (2006).
67. T. Kuila, A. K. Mishra, P. Khanra, N. H. Kim, J. H. Lee, *Nanoscale* **5**, 52 (2013).
68. S. Krishnamurthy, I. V. Lightcap, P. V. Kamat, *J. Photochem. Photobio. A: Chem.* **221**, 214 (2011).
69. B. Gadgil, P. Damlin, M. Heinonen, C. Kvarnström, *Carbon* **89**, 53 (2015).
70. S. Eigler, A. Hirsch, *Angew. Chem. Int. Ed.* **53**, 7720 (2014).
71. K. Koshika, N. Sano, K. Oyaizu, H. Nishide, *Chem. Commun.* **7**, 836 (2009).
72. T. Suga, H. Konishi, H. Nishide, *Chem. Commun.* **17**, 1730 (2007).
73. K. Koshika, N. Chikushi, N. Sano, K. Oyaizu, H. Nishide, *Green Chem.* **12**, 1573 (2010).
74. K. Koshika, N. Sano, K. Oyaizu, H. Nishide, *Macromol. Chem. Phys.* **210**, 1989 (2009).
75. H. Bai, C. Li, X. Wang, G. Shi, *Chem. Commun.* **46**, 2376 (2010).
76. X. Fan, W. Peng, Y. Li *et al.*, *Adv. Mater.* **20**, 4490 (2008).
77. Y. Cao, J. Zhang, J. Feng, P. Wu, *ACS Nano* **5**, 5920 (2011).
78. C. Chen, W. Cai, M. Long *et al.*, *ACS Nano* **4**, 6425 (2010).
79. C. Huang, H. Bai, C. Li, G. Shi, *Chem. Commun.* **47**, 4962 (2011).
80. X. Chen, G. Wu, J. Chen *et al.*, *J. Am. Chem. Soc.* **133**, 3693 (2011).
81. H. Wang, Q. Zhang, X. Chu *et al.*, *Angew. Chem. Int. Ed.* **50**, 7065 (2011).
82. B. Konkena, S. Vasudevan, *J. Phys. Chem. Lett.* **3**, 867 (2012).
83. C. Werner U. König *et al.*, *Colloids Surf. A: Physicochem. Eng. Asp.* **159**, 519 (1999).
84. H. J. Keh, J. L. Anderson, *J. Fluid Mech.* **153**, 417 (2006).
85. A. R. Minerick, A. E. Ostafin, H.-C. Chang, *Electrophoresis* **23**, 2165 (2002).
86. D. Erickson, D. Li, *Langmuir* **18**, 1883 (2002).
87. A. Sze, D. Erickson, L. Ren, D. Li, *J. Colloid Interface Sci.* **261**, 402 (2003).
88. M. Gallei, R. Klein, M. Rehahn, *Macromolecules* **43**, 1844 (2010).
89. E. S. Yang, M.-S. Chan, A. C. Wahl, *J. Phys. Chem.* **79**, 2049 (1975).
90. C. U. Pittman, J. C. Lai, D. P. Vanderpool, M. Good, R. Prado, *Macromolecules* **3**, 746 (1970).
91. A.-R. Allouche, *J. Comput. Chem.* **32**, 174 (2011).
92. A. Bansal, H. Yang, C. Li *et al.*, *Nat. Mater.* **4**, 693 (2005).
93. F. Yang, Y. Liu, L. Gao, J. Sun, *J. Phys. Chem. C* **114**, 22085 (2010).
94. D. Li, M. B. Muller, S. Gilje, R. B. Kaner, G. G. Wallace, *Nat. Nano* **3**, 101 (2008).
95. E. Dickinson, *J. Chem. Tech. Biotech.* **45**, 328 (1989).
96. G. Xin, H. Wang, N. Kim *et al.*, *Nanoscale* **4**, 405 (2012).

97. X. Li, W. Cai, J. An *et al.*, *Science* **324**, 1312 (2009).
98. M. Keidar, A. Shashurin, O. Volotskova *et al.*, *Phys. Plasmas* **17**, 057101 (2010).
99. M. Alexander, V. Roumen, S. Koen *et al.*, *Nanotechnology* **19**, 305604 (2008).
100. T. Szabó, O. Berkesi, P. Forgó *et al.*, *Chem. Mater.* **18**, 2740 (2006).
101. S. Stankovich, D. A. Dikin, R. D. Piner *et al.*, *Carbon* **45**, 1558 (2007).
102. O.-K. Park, M. G. Hahn, S. Lee *et al.*, *Nano Lett.* **12**, 1789 (2012).
103. Z. Tiannan, C. Feng, L. Kai *et al.*, *Nanotechnology* **22**, 045704 (2011).
104. Z.-J. Fan, W. Kai, J. Yan *et al.*, *ACS Nano* **5**, 191 (2011).
105. X. Mei, J. Ouyang, *Carbon* **49**, 5389 (2011).
106. Z. Fan, K. Wang, T. Wei *et al.*, *Carbon* **48**, 1686 (2010).
107. H.-L. Guo, X.-F. Wang, Q.-Y. Qian *et al.*, *ACS Nano* **3**, 2653 (2009/09/22, 2009).
108. Y. Shao, J. Wang, M. Engelhard *et al.*, *J. Mater. Chem.* **20**, 743 (2010).
109. N. F. Sheppard, R. C. Tucker, C. Wu, *Anal. Chem.* **65**, 1199 (1993).
110. S. Eigler, M. Enzelberger-Heim, S. Grimm *et al.*, *Adv. Mater.* **25**, 3583 (2013).
111. C. E. Halbig, T. J. Nacken, J. Walter *et al.*, *Carbon* **96**, 897 (2016).
112. L. G. Cançado, A. Jorio A, E. H. M. Ferreira *et al.*, *Nano Lett.* **11**, 3190 (2011).
113. M. M. Lucchese, F. Stavale, E. H. M. Ferreira *et al.*, *Carbon* **48**, 1592 (2010).
114. S. Eigler, F. Hof, M. Enzelberger-Heim *et al.*, *J. Phys. Chem. C* **118**, 7698 (2014).
115. S. Pei, H.-M. Cheng, *Carbon* **50**, 3210 (2012).
116. J. Yang, S. Gunasekaran, *Carbon* **51**, 36 (2013).
117. I. Jureviciute, S. Bruckenstein, A. R. Hillman, *J. Electroanal. Chem.* **488**, 73 (2000).
118. M. D. Levi, N. Levy, S. Sigalov *et al.*, *J. Am. Chem. Soc.* **132**, 13220 (2010).
119. W.-Y. Tsai, P.-L. Taberna, P. Simon, *J. Am. Chem. Soc.* **136**, 8722 (2014).
120. H. C. De Long, D. A. Buttry, *Langmuir* **8**, 2491 (1992).
121. D. C. Apodaca, R. B. Pernites, R. R. Ponnampati *et al.*, *ACS Appl. Mater. Interfaces* **3**, 191 (2011).
122. D. Johannsmann, *Phys. Chem. Chem. Phys.* **10**, 4516 (2008).
123. A. R. Hillman, N. A. Hughes, S. Bruckenstein, *J. Electrochem. Soc.* **139**, 74 (1992).
124. P. T. Varineau, D. A. Buttry, *J. Phys. Chem.* **91**, 1292 (1987).
125. N. Shpigel, M. D. Levi, S. Sigalov *et al.*, *Nat. Mater* **15**, 570 (2016).
126. N. Nitta, G. Yushin, *Part. Part. Syst. Charact.* **31**, 317 (2014).
127. J. Song, M. A. Hempenius, H. Jing Chung, G. Julius Vancso, *Nanoscale* **7**, 9970 (2015).
128. A. Anne, E. Cambril, A. Chovin, C. Demaille, *Analyt. Chem.* **82**, 6353 (2010).
129. S. Eigler, S. Grimm, M. Enzelberger-Heim *et al.*, *Chem. Commun.* **49**, 7391 (2013).
130. S. Eigler, *Phys. Chem. Chem. Phys.* **16**, 19832 (2014).
131. C. Tonhauser, M. Mazurowski, M. Rehahn, M. Gallei, H. Frey, *Macromolecules* **45**, 3409 (2012).
132. M. Mazurowski, M. Gallei, J. Li *et al.*, *Macromolecules* **45**, 8970 (2012).
133. H. Feng, R. Cheng, X. Zhao, X. Duan, J. Li, *Nat. Commun.* **4**, 1539 (2013).
134. X. Li, G. Zhang, X. Bai *et al.*, *Nat. Nano.* **3**, 538 (2008).
135. G. Gritzner, J. Kuta, in *Pure and Applied Chemistry*. (1984), vol. 56, pp. 461.
136. C. Iwakura, T. Kawai, M. Nojima, H. Yoneyama, *J. Electrochem. Soc.* **134**, 791 (1987).

Abbreviation

PVFc	Poly(VinylFerrocene)	cm	centimeter
AFM	Atomic Force Microscopy	Ag/AgCl	silver/silver chloride
EC	Electrochemical	Au	gold
MHz	MegaHertz	e	electron
G	Graphene	LiClO ₄	Lithium perchlorate
GO	Graphene oxide	s	second
rGO	reduced Graphene Oxide	TGA	thermogravimetric analysis
MV ⁺⁺	Methyl Viologen dichloride	wt	weight
I	Current	MeCN	Acetonitrile
t	time	EC	Ethylene Carbonate
V	Voltage	DMC	Dimethyl Carbonate
Wh	Watt hour	mC	milliCoulomb
kg	kilogram	CHCl ₃	Chloroform
mAh	milliampere hour	ET	Electron Transfer
LIB	Lithium Ion Battery	M	Molar
IoT	Internet of Things	mmol	millimoles
Fc	Ferrocene	UV-Vis	UltraViolet-Visible
J	Joule	v	Scan rate
HOMO	Highest Occupied Molecular Orbital	LUMO	Lowest Unoccupied Molecular Orbital
Mw	Molecular weight	ET	Electron transfer
CV	Cyclic Voltammetry	LiCoO ₂	Lithium Cobalt Oxide
CC	Current Collector	LiMn ₂ O ₄	Lithium Manganese Oxide
GC	Glassy Carbon	LiFePO ₄	Lithium Iron Phosphate
ITO	Indium Tin Oxide	S	Sulfure
FTO	Fluorine doped Tin Oxide	V	vanadium
CNT	Carbon NanoTube	PF ₆	Hexafluorophosphate
ζ	Zeta Potential	Vio	Viologen
ε	dielectric constant	AgNO ₃	Silver Nitrate
η	viscosity	kDa	kiloDalton
f(K _a)	Henry's function	MWCO	Molecular Weight Cut-Off
rpm	revolutions per minute	XRD	X-Ray Diffraction
CVD	Chemical Vapor Deposition	f	frequency
IME	Interdigitated Microsensor Electrode	EQCM	Electrochemical Quartz Crystal Microbalance
Ω	Ohm	μm	micrometer
nm	nanometer	SCE	Saturated calomel electrode

Curriculum Vitae

Name: Seyyed Mohsen Beladi Mousavi
Date of Birth: 22 – 09 – 1984
Place of Birth: Ahvaz, Iran
Citizenship: Iranian

EDUCATION

University of Osnabrück, Germany
PhD, Organic chemistry and molecular electrochemistry 2012 - present

University of Sistan and Baluchestan, Zahedan, Iran
MSc, Organic chemistry 2008 – 2011

Imam Khomeini International University (IKIU), Qazvin, Iran
BSc, Chemistry 2003 - 2007

PUBLICATION

Poly(vinylferrocene)–Reduced Graphene Oxide as a High Power/High Capacity Cathodic Battery Material. *Adv. Energy Mater.* (2016), S. M. Beladi-Mousavi, S. Sadaf, L. Walder, M. Gallei, C. Rüttiger, S. Eigler and C. E. Halbig

Surface Oxidation of Stainless Steel: Oxygen Evolution Electrocatalysts with High Catalytic activity. *ACS Catalysis*, (2015) H. Schäfer, S. M. Beladi-Mousavi, L. Walder, et. al.

Oxidized Mild Steel S235: An Efficient Anode for Electrocatalytically Initiated Water Splitting. *CHEMSUSCHEM*, (2015), H. Schäfer, K. Küpper, J. Wollschläger, N. Kashaev, J. Hardege, L. Walder, S.M. Beladi-Mousavi, et. al.

PolyTEMPO and polyviologen on carbon nanotubes: syntheses, structures and organic battery applications. *European Polymer Journal*, (2013), L. Cao, S. Sadaf, S. M. Beladi-Mousavi, L. Walder.

PATENT

A patent application on organic battery materials. *Submitted*, (Oct. 2016), S. M. Beladi-Mousavi, L. Walder.

Declaration

I hereby declare that this thesis is the summary of my Ph.D. work and has not been submitted to any other university. All the sources and materials used in this thesis are duly acknowledged and cited.

Osnabrück, November 2016

Seyyed Mohsen Beladi Mousavi